NASA

TECHNICAL MEMORANDUM
X - 646

THE EFFECTS OF SOME VARIATIONS IN LAUNCH-VEHICLE NOSE

SHAPE ON STEADY AND FLUCTUATING PRESSURES

AT TRANSONIC SPEEDS

By Charles F. Coe

Ames Research Center
Moffett Field, Calif.

NATIONAL AERONAUTICS AND SPACE ADMINISTRATION

WASHINGTON   March 1962

K

NATIONAL AERONAUTICS AND SPACE ADMINISTRATION

TECHNICAL MEMORANDUM X-646

THE EFFECTS OF SOME VARIATIONS IN LAUNCH-VEHICLE NOSE

SHAPE ON STEADY AND FLUCTUATING PRESSURES

AT TRANSONIC SPEEDS

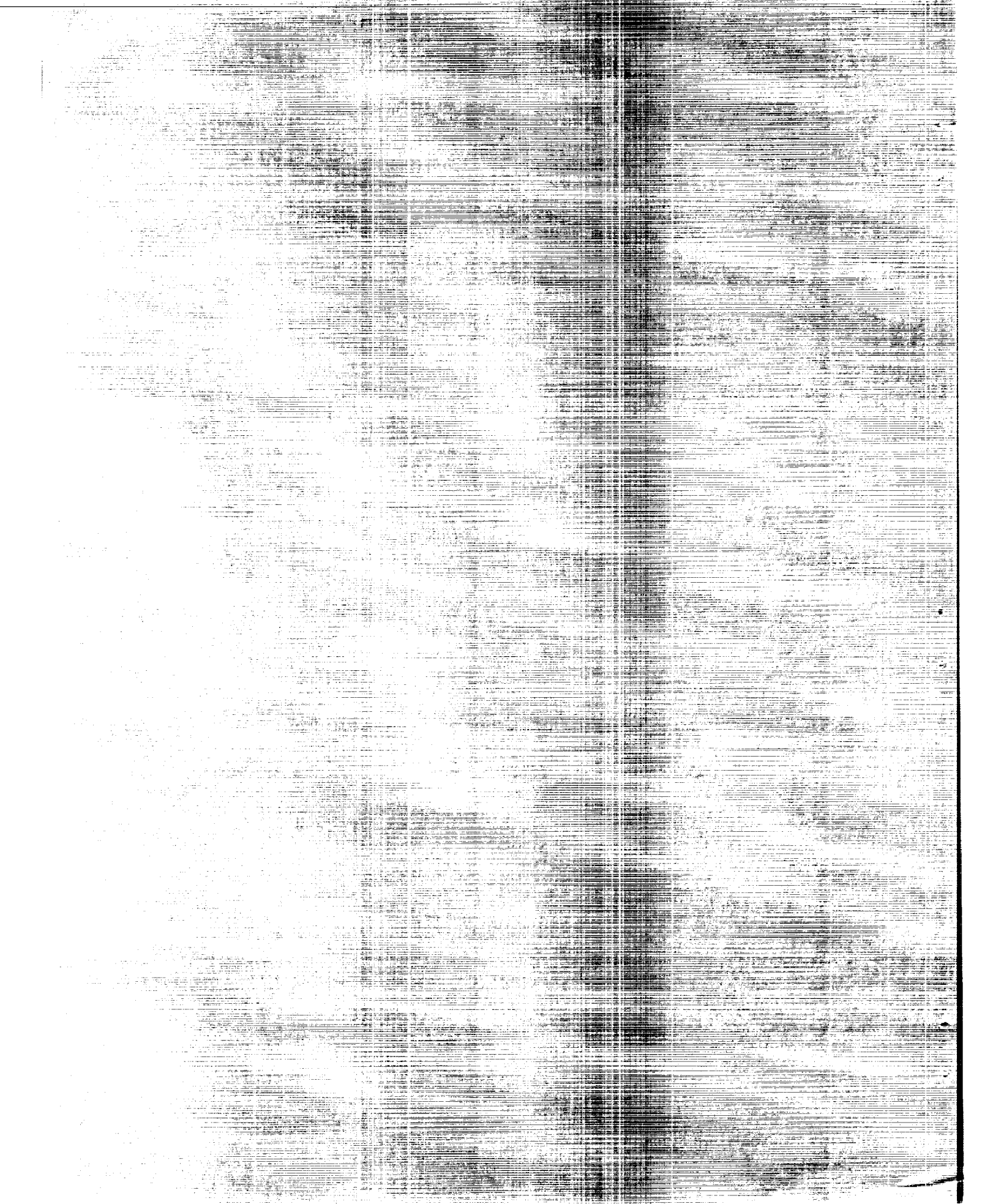By Charles F. Coe

SUMMARY

Steady and fluctuating pressures have been measured along the top center lines of five bodies of revolution within the Mach number range from 0.6 to 1.2. Three models had ellipsoidal noses with fineness ratios of 2 on afterbodies which were cylindrical or converging. One model had a fineness-ratio-1/2 ellipsoidal nose, and one model had a cone-cylinder nose with a diverging section in the afterbody.

The results of the investigation showed that pressure fluctuations and possible unsteady bending loads on a vehicle with a cylindrical body are small if the nose is sufficiently slender. Boattailing or a reduction in cross-sectional area following a slender nose results in separation of flow and extensive regions of pressure fluctuations. The sharpness of the area reduction affects the Mach number range over which these pressure fluctuations occur.

The maximum pressure fluctuations on a staged-vehicle model having cylindrical sections of different diameter and equal preceding cone angles were about the same on either diameter section. Although results from similar model sections of different diameters indicated little effect of size on the maximum fluctuations that occurred in the region of the shock wave, definite conclusions cannot be drawn insofar as scaling to a full-scale vehicle is concerned.

Comparison of power spectral densities of the fluctuations on all the models tested indicated that they are dependent upon the location within a particular type of flow and are not peculiar to a specific model profile.

INTRODUCTION

References 1 and 2 show that significant fluctuations of pressure can occur on bodies of revolution within the transonic speed range. These fluctuations which originated at the location of the normal shock wave and within regions of separation can cause buffeting of an exiting space vehicle. However, whether buffeting has caused failures of space vehicles during launch has not to the author's knowledge been definitely established. It has been recognized though that the buffet loads must be considered in the design of the space-vehicle structure.

The problem of predicting structural response to unsteady aerodynamic loads with reasonable accuracy is a difficult one. Calculations of the buffet loads on the Atlas-Able-V and Mercury-Atlas vehicles have been attempted (refs. 3 and 4), but the spacial correlation of the local pressure fluctuations were unknown for the aerodynamic input. The possibility suggested by the results of reference 1, that coupling may occur between the unsteady forces and motion, also could not be taken into account due to the lack of necessary experimental information. Since investigations to measure the over-all time correlated buffet loads and the effects of motion are time consuming, the buffet problem should also be examined more expeditiously by studying the effect of shape parameters on fluctuating pressures to indicate which shapes have low fluctuating pressures.

A research program has been undertaken at Ames Research Center to investigate both the over-all buffet loads and the local steady and fluctuating pressures on various body shapes. The results of the first tests of two configurations are contained in reference 1. Measurements of steady and fluctuating pressures along the top center line of five additional bodies of revolution are presented herein to illustrate the effects of nose and afterbody shape and interstage flare.

NOTATION

C_p time-average pressure coefficient, $\dfrac{p - p_o}{q_o}$

$\Delta C_p(\text{RMS})$ coefficient of the root-mean-square fluctuation of pressure about the mean

M free-stream Mach number

Re Reynolds number

D maximum body diameter

p   local static pressure

p_o free-stream static pressure

p_t stagnation pressure

q_o free-stream dynamic pressure

f   frequency, cps

x   distance along body axis from nose

α angle of attack

APPARATUS AND TECHNIQUE

Models

Profiles of the five models that were tested are shown in figure 1 as models I through V. Models VI and VII (Centaur and Able-V shapes), for which similar tests were conducted with results appearing in reference 1, are also shown to indicate their relative profiles. Models I and II had ellipsoidal noses with fineness ratios of 1/2 and 2. They were selected to investigate the effects of nose shape on local pressure fluctuations since considerable static-force and pressure-distribution data and some dynamic-stability data are available from models incorporating these nose shapes in references 5 and 6. Models III and IV had the same ellipsoidal nose shape as model II but had different afterbodies to determine the effect of body convergence. The general profile of model III was similar to that of model VII (Able-V shape) except that it had a slightly more slender ellipsoidal nose fitted tangent to the converging afterbody. The Able V had a short cylindrical section ahead of its converging afterbody. Model V was tested to examine the influence of a second stage of a vehicle and an interstage flare on the local flow over the first stage. The first stage was a half-scale model of the original cone-cylinder combination of model VI.

Sketches of models I through V showing pertinent dimensions and the locations of static-pressure orifices and pressure transducers are in figure 2. Orifices for these five models were located only along the top center line. The transducers were offset to the right of their adjacent orifices 3/8 inch on the models with 9.12-inch maximum diameters (I, II, and V), and 1/2 inch on the models with 12-inch maximum diameters (III and IV). The angular offset amounts to approximately 4.75° at the maximum diameters, but varies with model radius. For convenience the transducers will be referred to as being located along the top center lines of the models.

All the models can be considered to be of rigid construction and were rigidly attached to the wind-tunnel sting-support system. To take advantage of existing model components, combinations of structural materials were used. The instrumented portions of models I and II and of the larger diameter section of model V were of glass-fiber construction braced with steel rings. A solid wood body extension with a length equal to two diameters was used with each of these models. Models III and IV and the nose and interstage-flare sections of model V were constructed of wood hollowed at the core to make room for necessary pressure tubes and wires. Shake tests of the model support system with models III, IV, and V installed were performed, and the measured resonant frequencies are listed in table I. Shake tests were not made with models I and II; however, it would be expected that the resonant frequencies would be in the same general range as measured for the other models since the total mass and mass distribution of the model and model-support system were nearly the same for all models.

Wind Tunnel and Instrumentation

Tests were conducted in the Ames 14-Foot Transonic Wind Tunnel through a Mach number range from 0.60 to about 1.20.[1] This tunnel operates at a constant stagnation pressure, approximately atmospheric but, as a result of some control of stagnation temperature, Reynolds number varies with Mach number as illustrated by the shaded band in figure 3.

The pressure transducers and electronic components used for recording the pressure fluctuations were the same as in reference 1. The transducers were 0.250-inch diameter and were mounted so that their diaphragms were flush with the model surface. The back side of the diaphragm of each transducer was referenced to the time-average static pressure from its adjacent orifice so that the transducers responded only to the fluctuations of pressure about the mean. A steady reference pressure was insured by the use of a combined tube length of about 150 feet which connected the transducer and its adjacent orifice.

Procedure

The calibration procedure and method of data reduction were the same as described in reference 1. The procedure for conducting the tests of the Centaur model of reference 1 was also used for this investigation; that is, tests were conducted at constant angles of attack and the Mach

[1]A minor exception was a very brief test of model VI in the 11-foot test section of the Ames Unitary Plan Wind Tunnel to obtain the effects of Reynolds number on the pressure fluctuations in the region of the shock wave.

number was varied within the test limits from 0.60 to about 1.20. In the range of Mach numbers where significant pressure fluctuations occurred in the region of the normal shock wave $(0.7 < M < 1)$, the Mach number was adjusted in whatever increments were required to locate the maximum intensities at successive pressure-transducer stations along the top of the models.

RESULTS AND DISCUSSION

Intensities of Pressure Fluctuations

The longitudinal distributions of the pressure fluctuations as measured along the top center lines of the models are in figures 4 through 8.

Effect of nose bluntness.- Examination of figures 4 and 5 shows that the pressure fluctuations were much smaller on model II than on model I. As with the cone-cylinder combination of the Centaur model (ref. 1), the fluctuations on model II were confined to the region of the shock wave. Blunting the nose to an ellipsoid of fineness ratio 1/2 resulted in severe separation (see fig. 9) with significant fluctuations of pressure extending over much of the model surface. The largest local fluctuations were measured on model I, $\Delta C_p(RMS) = 0.17$, at the forward boundary of the separation near the beginning of the cylindrical section. The lowest fluctuations measured in the region of the shock wave for any of the models occurred on model II, $\Delta C_p = 0.068$. Since the fluctuations in the region of the shock wave on model II were slightly lower than those measured on model VI (ref. 1), and since fluctuations due to separation are negligible on both models, it appears that an ellipsoidal nose with a fineness ratio of 2 could be substituted for the conical nose of model VI. A possible advantage of such a substitution could come from a gain of internal volume near the nose resulting in a shorter and possibly lighter weight space-vehicle payload shroud.

Since the nose on model II is sufficiently slender that fluctuations due to separation are negligible even at $\alpha = 8°$, it might be expected that separation would not occur for a nose substantially more blunt than the fineness-ratio-2 ellipsoid. Although pressure-fluctuation data have not been obtained for noses with degrees of bluntness between models I and II, shadowgraph pictures in figure 9 show that for a hemispherical nose there was separation at $\alpha = 0°$. The picture of the flow on the hemisphere-nose model was taken during tests for reference 5.

Effect of body convergence.- Results in figures 5, 6, and 7 for models II, III, and IV show the effect of convergence to smaller body

diameters. The three models had the same nose shape. Model II, serving
as a basis of comparison, had a cylindrical body while model III had a
6° 30' convergence and model IV, a 30° convergence. The results illus-
trate the advantage of avoiding boattailing or reduction in diameter
following a payload fairing. As previously indicated in connection with
the results from model II, figure 5 shows that fluctuations occurred only
in the region of the shock wave and that separation effects were negli-
gible. Although fluctuations due to separation also appear negligible
at $\alpha = 0^{\circ}$ when the slope of the body convergence is only 6° 30'
(model III, fig. 6), separation effects do appear at angles of 4° and 8°.
It is the large area over which these fluctuations extend that suggests
the possibility that unsteady normal forces can become large enough to
cause appreciable vehicle bending loads.

As the sharpness of the area reduction in a converging section is
increased, it can be seen in figure 7 that both the ranges of angle of
attack and Mach number are affected over which fluctuations due to
separation occur. Model IV was the only one which maintained separated
flow at supersonic Mach numbers.

Shadowgraph pictures which illustrate the effect of body convergence
on the flow are shown at $\alpha = 0^{\circ}$ and 8° in figure 10. The differences in
the pressure-fluctuation intensities which occurred within separated
regions (figs. 6 and 7) is not apparent from the shadowgraph pictures.

Effect of interstage flare.- The results from model V (fig. 8)
showed significant fluctuations occurring only in the region of the shock
wave behind the cone-cylinder junction of both stages. Tests at a few
Mach numbers at $\alpha = 12^{\circ}$ and 16° showed that separation effects were
small even through the extended angle-of-attack range. The dashed lines
in the distributions of the pressure fluctuations were faired to illus-
trate the approximate locations of the shock wave when it was between
transducer stations.

The intensities of the maximum fluctuations, which also appear in
figure 11 along with results from model VI, were affected only slightly
by staging. The fact that the intensities measured on the smaller
diameter section of model V were nearly as high as those measured on the
basic Centaur model (VI), indicates that increasing the Reynolds number
by a factor of 2 (due to a size variation) has little effect on the
maximum fluctuations that occur in the region of the shock wave. Power
spectral densities of these fluctuations, which appear in a later figure,
were also relatively unaffected by the change in model diameter. During
the brief tests of model VI in the 11-foot transonic wind tunnel, a few
test points were taken at 1 and 2 atmospheres total pressure (fig. 11(b))
which also showed the absence of a gross effect of Reynolds number (due
to a pressure variation) on the RMS intensities due to fluctuations which
occur in the region of the shock wave.

Steady Pressures

The longitudinal distributions of the steady and fluctuating
pressures are shown in figure 12 for selected Mach numbers illustrative
of the range of the tests. In the absence of suitable analytical means
for the determination of static pressures at transonic speeds, the
pressure distributions can be useful for the estimation of venting
requirements for various payload shapes and also for the estimation of
static bending loads on launch vehicle configurations. Although the
measurements of static pressure were obtained only along the top center
lines of the models, references 1 and 5 show the distributions of pressure
at various stations surrounding bodies of revolution from which peripheral
distributions can be estimated.

Some relationship between steady and fluctuating pressures is
apparent in figure 12. As previously indicated in reference 1, the
location of the maximum fluctuations in the region of the shock wave
can be determined from the position of the steep rising pressure gradient
through the shock. It also appears that the regions of fluctuations due
to separation can be located through examination of pressure distributions.

Power Spectral Densities

Power spectral densities for each of the models are presented in
figures 13 through 17. In general, the results show that the shapes of
the spectra were about the same as those obtained for the models in
reference 1. It appears that the shapes obtained were not peculiar to
a specific model profile, but were more dependent upon the particular
region of flow in which measurements were made, such as the region of a
shock wave or region of separation. Results in figure 15 at $x/D = 1.040$
and in figure 17 at $x/D = 0.817$, 3.309, and 1.634 are spectra that
occurred when a shock wave was just forming.[2] As the shock became well
established a greater amount of the energy was concentrated at the lower
frequencies (fig. 15, $x/D = 1.178$ and 1.311, and fig. 17, $x/D = 0.907$,
3.490, and 1.816). The spectral densities at $x/D = 1.311$ and 1.178 in
figure 15 approach a variation with frequency which is proportional
to $1/f^2$.

---

[2]The predominant peak near 190 cps appeared only in results obtained
in the 14-foot wind tunnel apparently as a coincidence of a model reso-
nant frequency and a very small disturbance in the stream (ref. 1). The
peak did not occur in spectra obtained during repeat tests in the 11-foot
wind tunnel, and thus can be disregarded when the over-all power-spectrum
shape is considered.

The shape of the spectra within separated regions seems to vary depending upon the location of the transducer with respect to the separation point. Near the separation point, for example, (fig. 13, $x/D = 0.251$) the spectral density was higher at lower frequencies and approached the $1/f^2$ variation with frequency. At stations which were progressively rearward from the separation point (fig. 13, $x/D = 0.580$ and 1.455, or fig. 16) the low frequency content diminished and the spectra were noticeably flatter throughout the recorded frequency range.

CONCLUSIONS

Measurements at transonic speeds of the steady and fluctuating pressures along the top center lines of five bodies of revolution have shown the following:

1. Pressure fluctuations and possible unsteady bending loads on a vehicle with a cylindrical body are small for either an ellipsoidal nose of fineness ratio 2 or a conical nose with a $14\text{-}1/2°$ half-cone angle.

2. Boattailing or reducing the cross-sectional area behind a slender nose results in separation of flow with the consequence that pressure fluctuations can occur over extensive areas on a vehicle.

3. The sharpness of the area reduction in converging sections affects the Mach number range over which unsteady pressures occur.

4. The maximum pressure fluctuations on a model with an interstage flare were approximately the same on cylindrical sections of different diameters following equal preceding cone angles.

5. Power spectral densities are dependent upon the location within a particular type of flow and are not peculiar to a specific model profile.

Ames Research Center
National Aeronautics and Space Administration
Moffett Field, Calif., Nov. 7, 1961

REFERENCES

1. Coe, Charles F.: Steady and Fluctuating Pressures at Transonic
   Speeds on Two Space-Vehicle Payload Shapes. NASA TM X-503, 1961.

2. Gall, E. S., and Kaupp, H., Jr.: Fluctuating Pressure Measurements
   on a 32-Percent Scale Model of the Mercury Capsule, Adapter, and
   Nose Portion of the Atlas Booster at Transonic Speeds.
   AEDC-TN-61-10, Feb. 1961.

3. Goldberg, A. P., and Wood, J. D.: Dynamic Loads in the Atlas-Able 5
   During Transonic Buffeting. STL/TM-60-0000-19075, 22 Aug. 1960.

4. Goldberg, Arthur P., and Adams, Richard H.: Mercury-Atlas Buffeting
   Loads at Transonic and Low Supersonic Speeds. STL/TR-60-0000-AS431,
   28 Nov., 1960.

5. Cleary, Joseph W.: The Effects of Nose Bluntness on the Flow
   Separation and Longitudinal Characteristics of Ellipsoidal-Nosed
   Cylinder-Flare Models at Transonic Speeds. NASA TM X-370, 1960.

6. Emerson, Horace F., and Robinson, Robert C.: The Transonic Damping
   in Pitch of Three Cylinder-Flare Models With Various Degrees of
   Nose Bluntness. NASA TM X-368, 1960.

TABLE I.- MODEL RESONANT FREQUENCIES

Model III	Model IV	Model V
10.7	10.4	8.8
30	29	27
61	60	46
117	115	72
191	191	86
281	270	189
		241

A
5
5
5
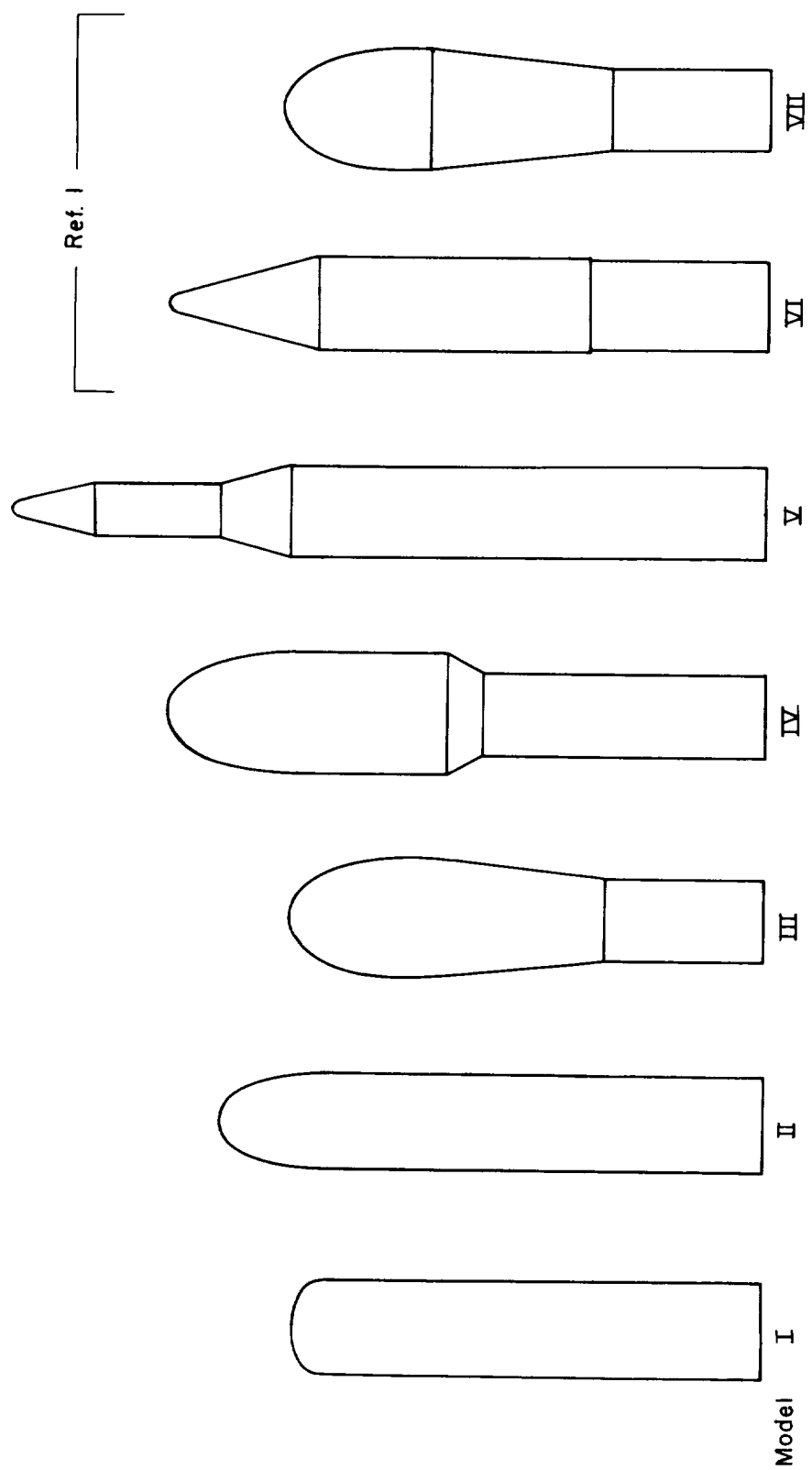
Figure 1.- Profiles of models tested.
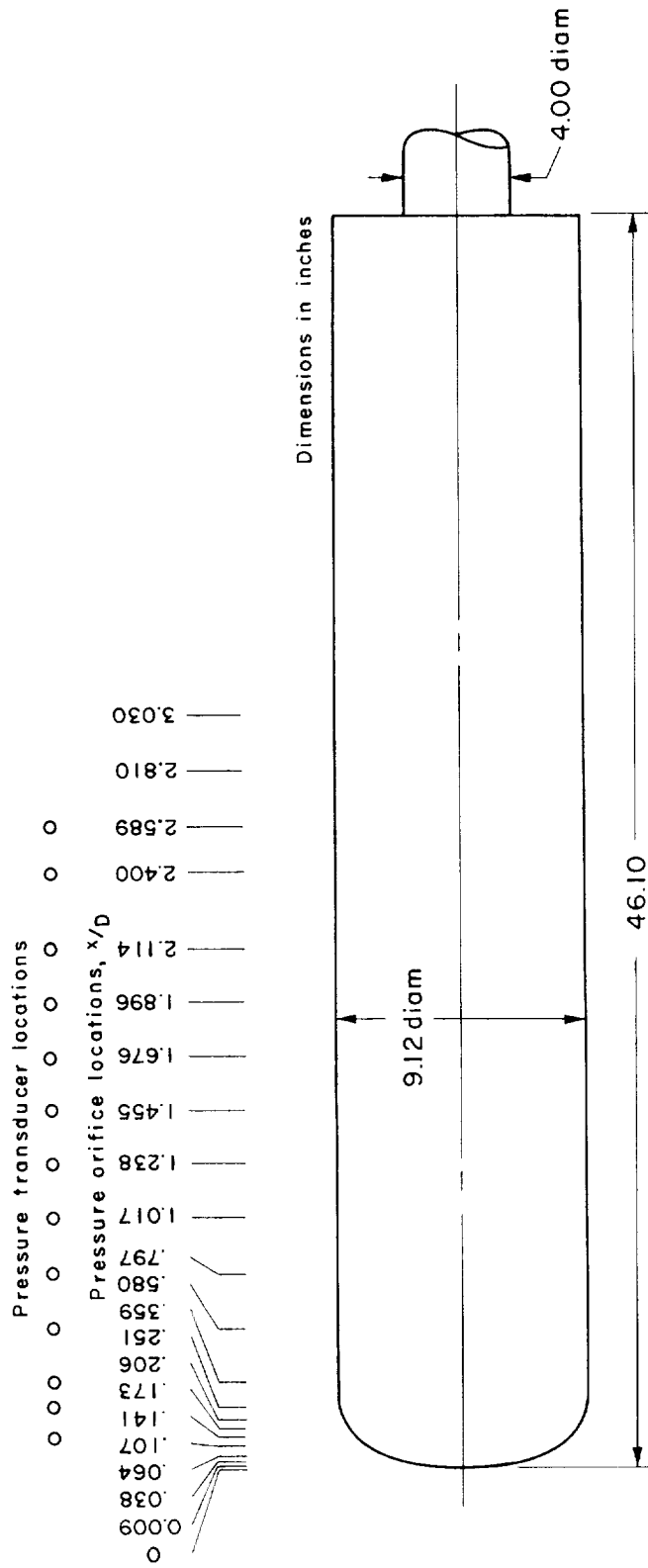
(a) Fineness-ratio-1/2 ellipsoidal nose on cylindrical body (model I).

Figure 2.- Sketches of models showing pertinent dimensions and locations of the static-pressure orifices and pressure transducers.

13

(b) Fineness-ratio-2 ellipsoidal nose on cylindrical body (model II).
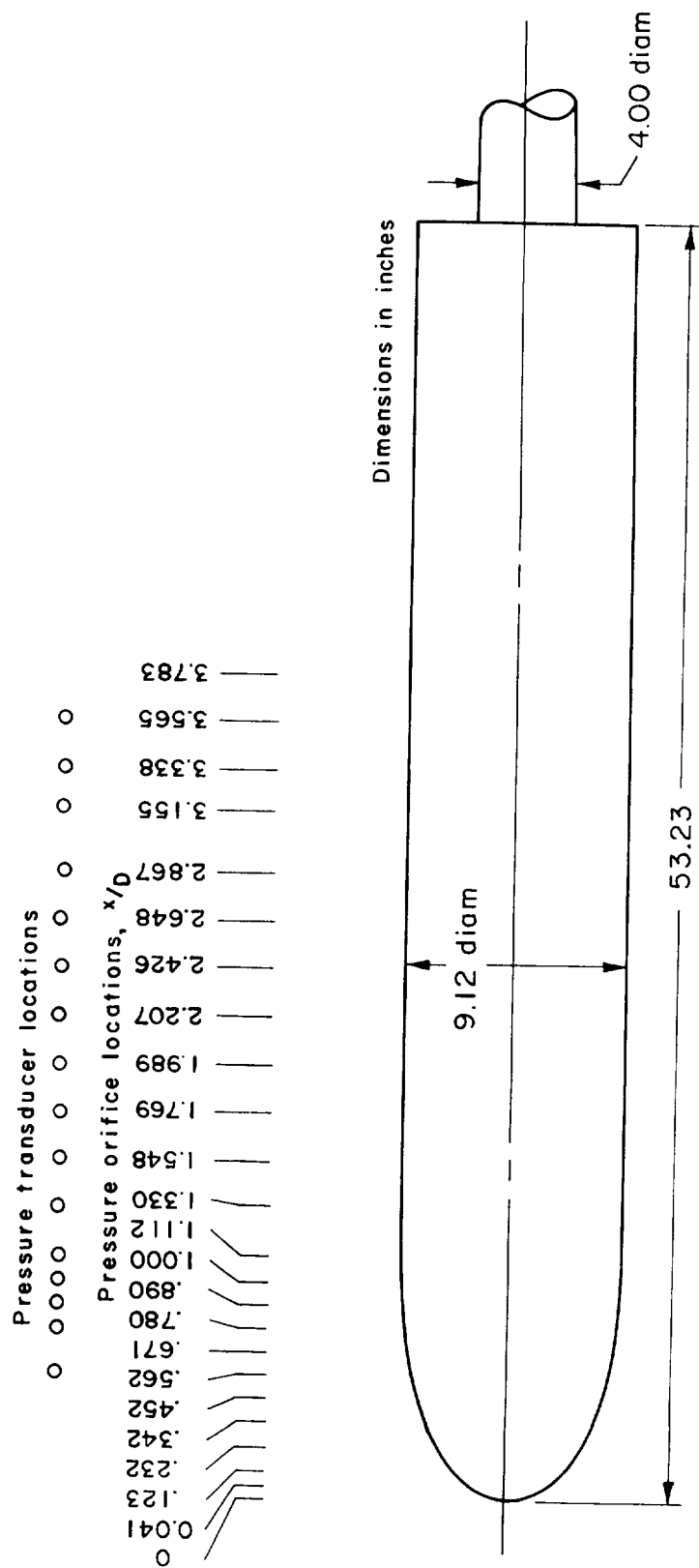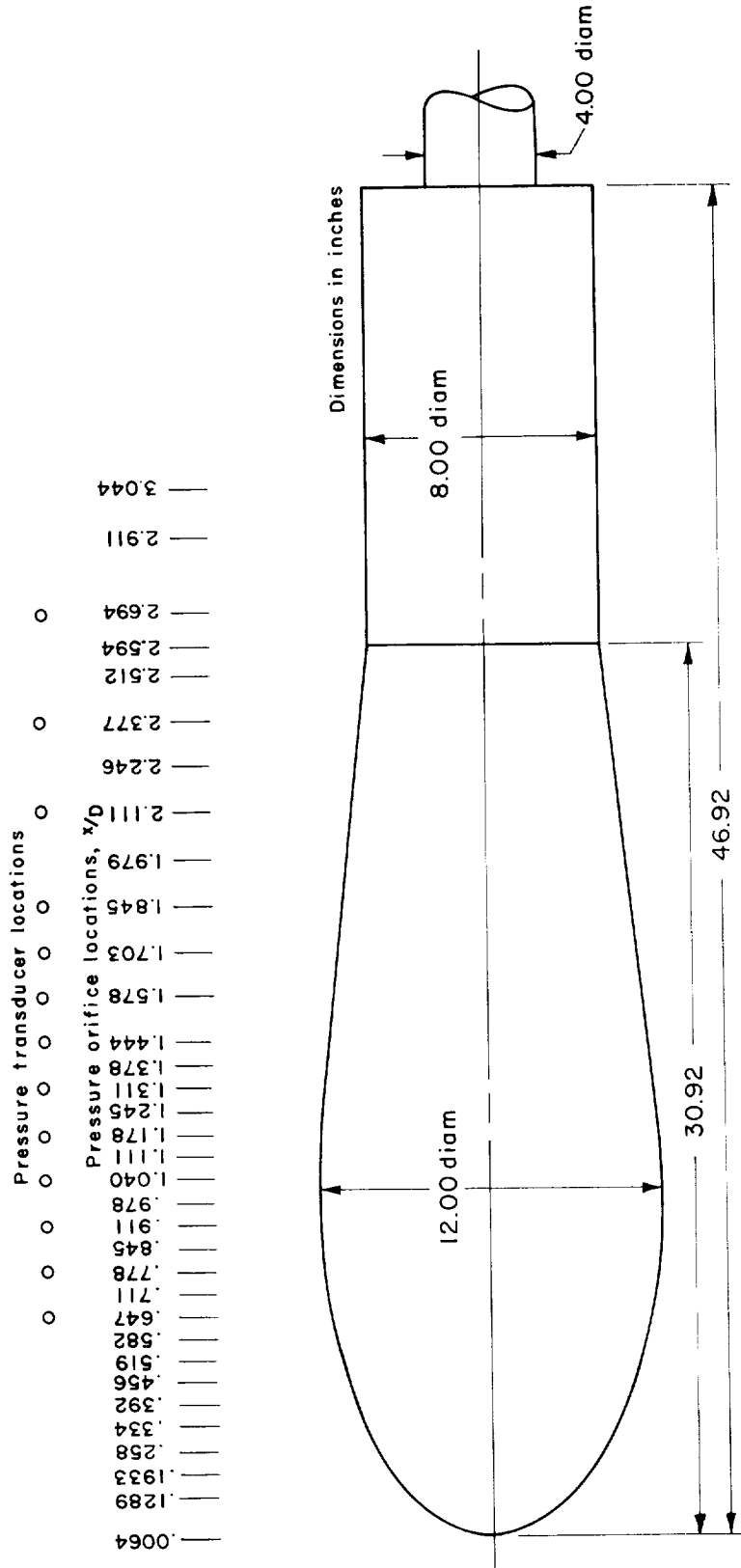
Figure 2.- Continued.

(c) Fineness-ratio-2 ellipsoidal nose on 6° 30' converging body section (model III).

Figure 2.- Continued.

15

Pressure transducer locations

Pressure orifice locations, x/D

3.40
3.20
3.00
2.88
2.70
2.60
2.50
2.45
2.38
2.30
2.20
2.10
2.00
1.845
1.703
1.578
1.444
1.378
1.311
1.245
1.178
1.111
1.045
.978
.911
.778
.647
.519
.392
0.258

Dimensions in inches

4.00 diam

8.00 diam

30°

58.92

30.92

12.00 diam
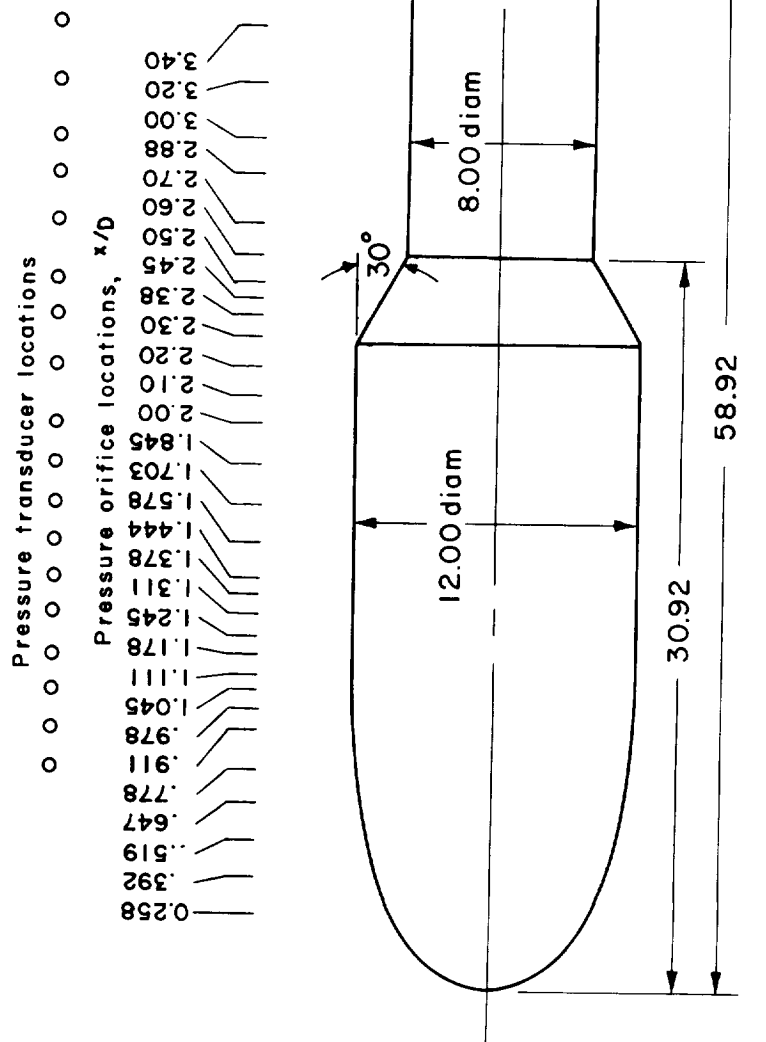
(d) Fineness-ratio-2 ellipsoidal nose on cylindrical body with 30° step (model IV).

Figure 2.- Continued.
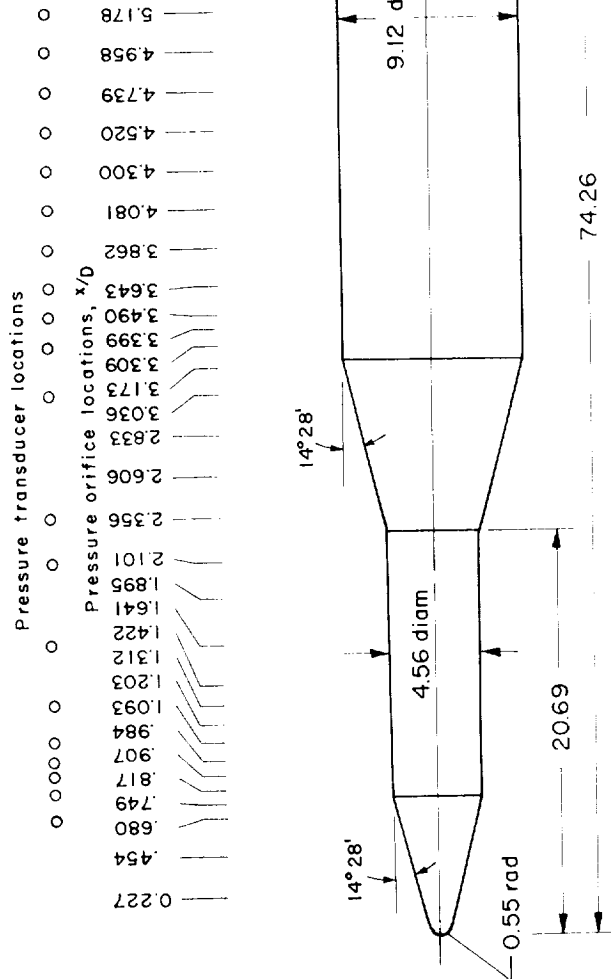
(e) Hemisphere-cone-cylinder staged vehicle (model V).

Figure 2.- Concluded.
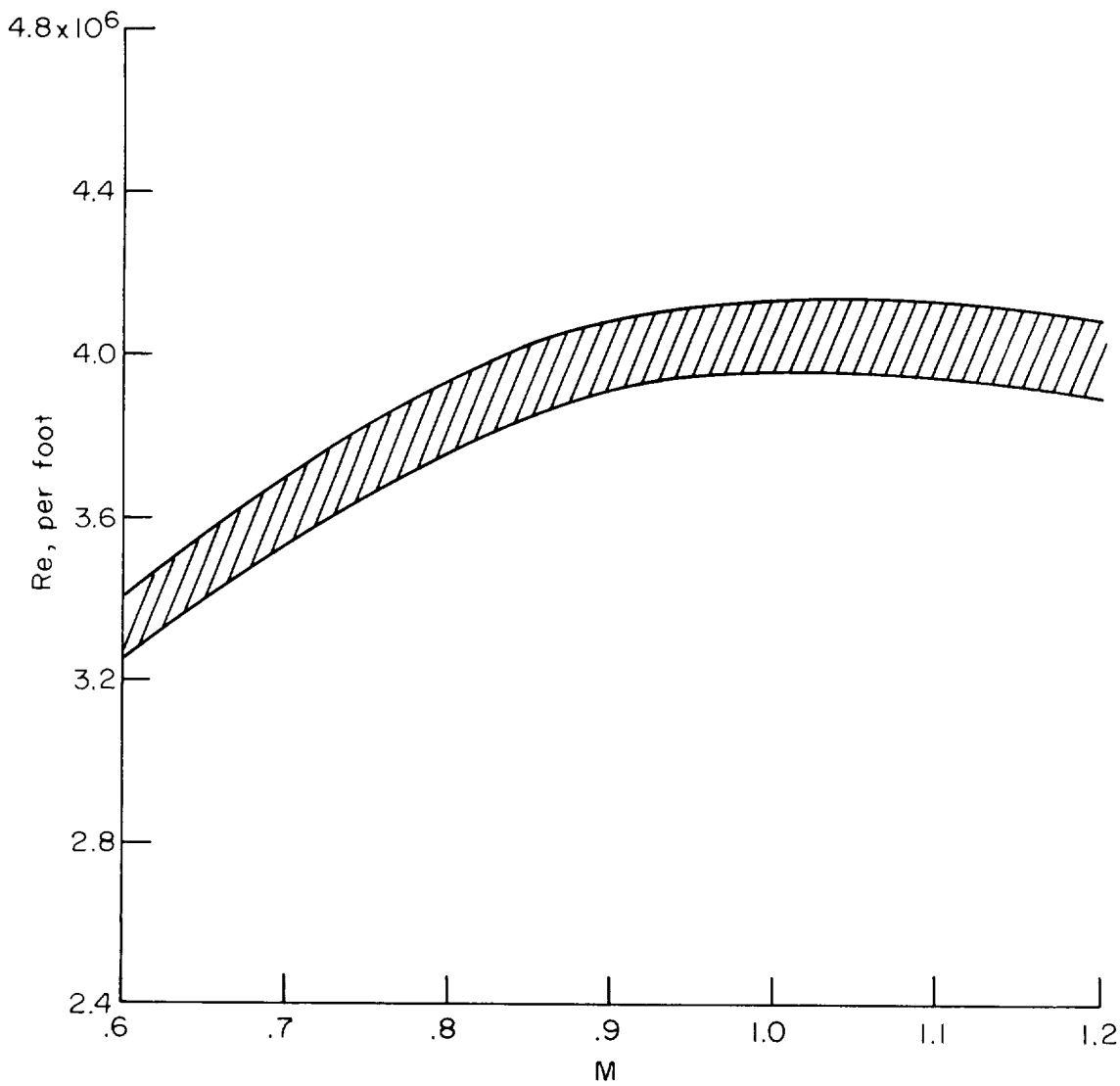
Figure 3.- Reynolds number range of the tests.

(a) $\alpha = 4°$
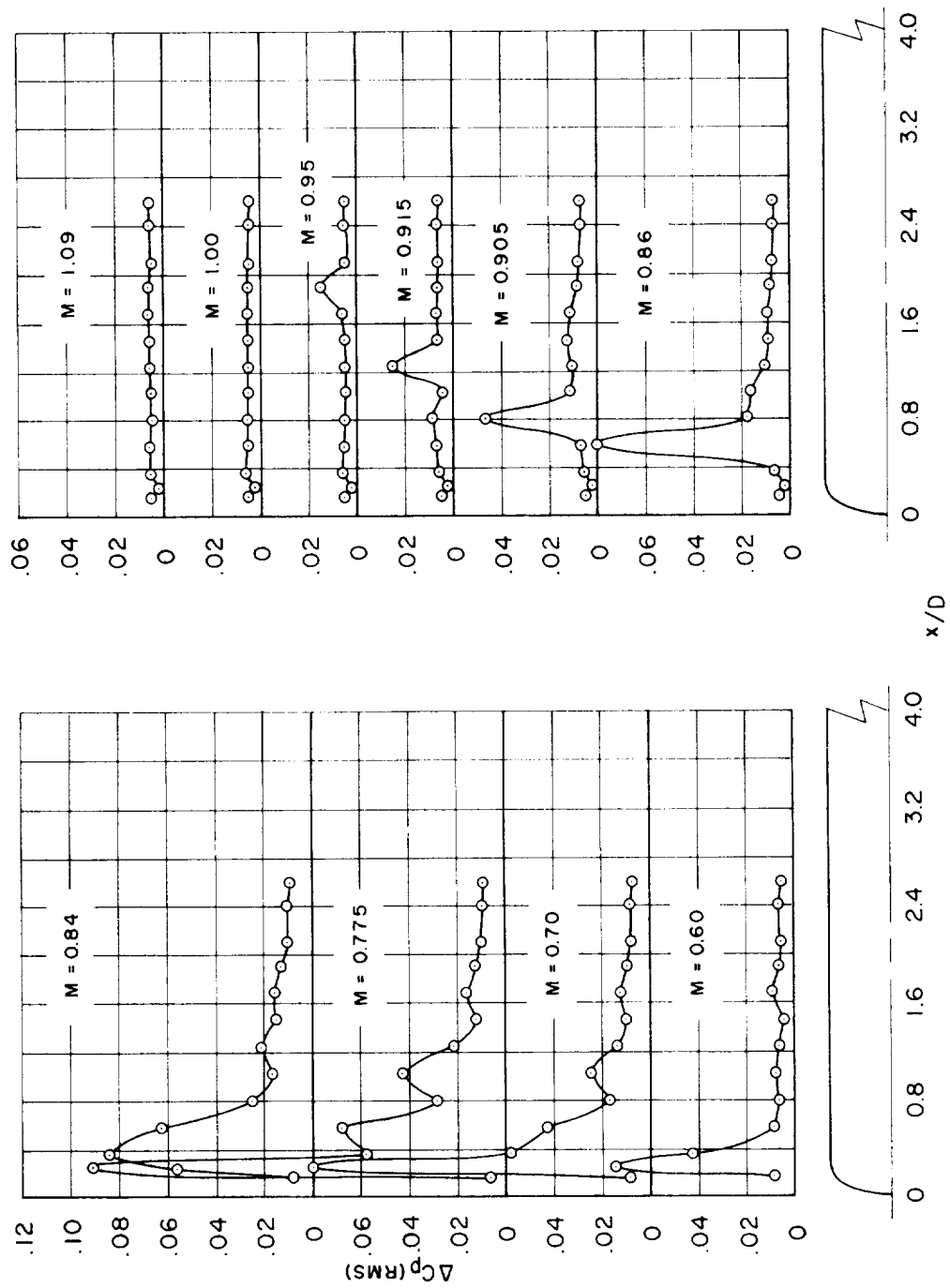
Figure 4.- Longitudinal distributions of the pressure fluctuations on model I.

(b) $\alpha = 0°$

Figure 4.- Continued.

.06

.04

.02

0

M = 1.09

.02

0

M = 1.00

.02

0

M = 0.96

.02

0

M = 0.93

.06

.04

.02

0

M = 0.905

0   0.8   1.6   2.4   3.2   4.0

.12

.10

.08

.06

.04

.02

0

M = 0.85

ΔC_p(RMS)

.06

.04

.02

0

M = 0.775

.04

.02

0

M = 0.70

.04

.02

0

M = 0.60

0   0.8   1.6   2.4   3.2   4.0

x/D

(c) $\alpha = 4^{\circ}$

Figure 4.- Continued.

M = 1.09

M = 1.00

M = 0.955

M = 0.93

M = 0.905

M = 0.85

M = 0.795

M = 0.70

M = 0.60

ΔC_p(RMS)

x/D

(d) $\alpha = 8^\circ$
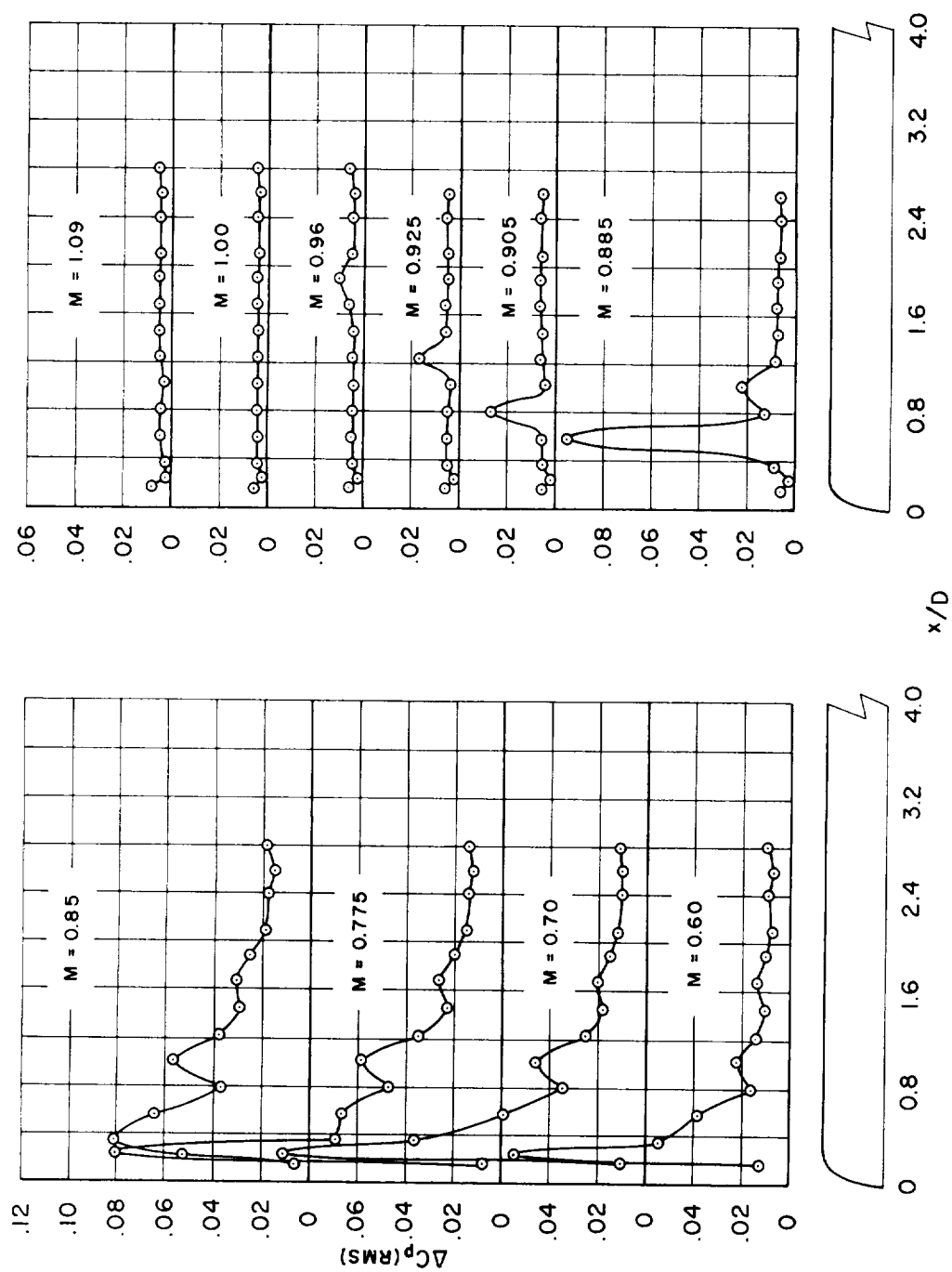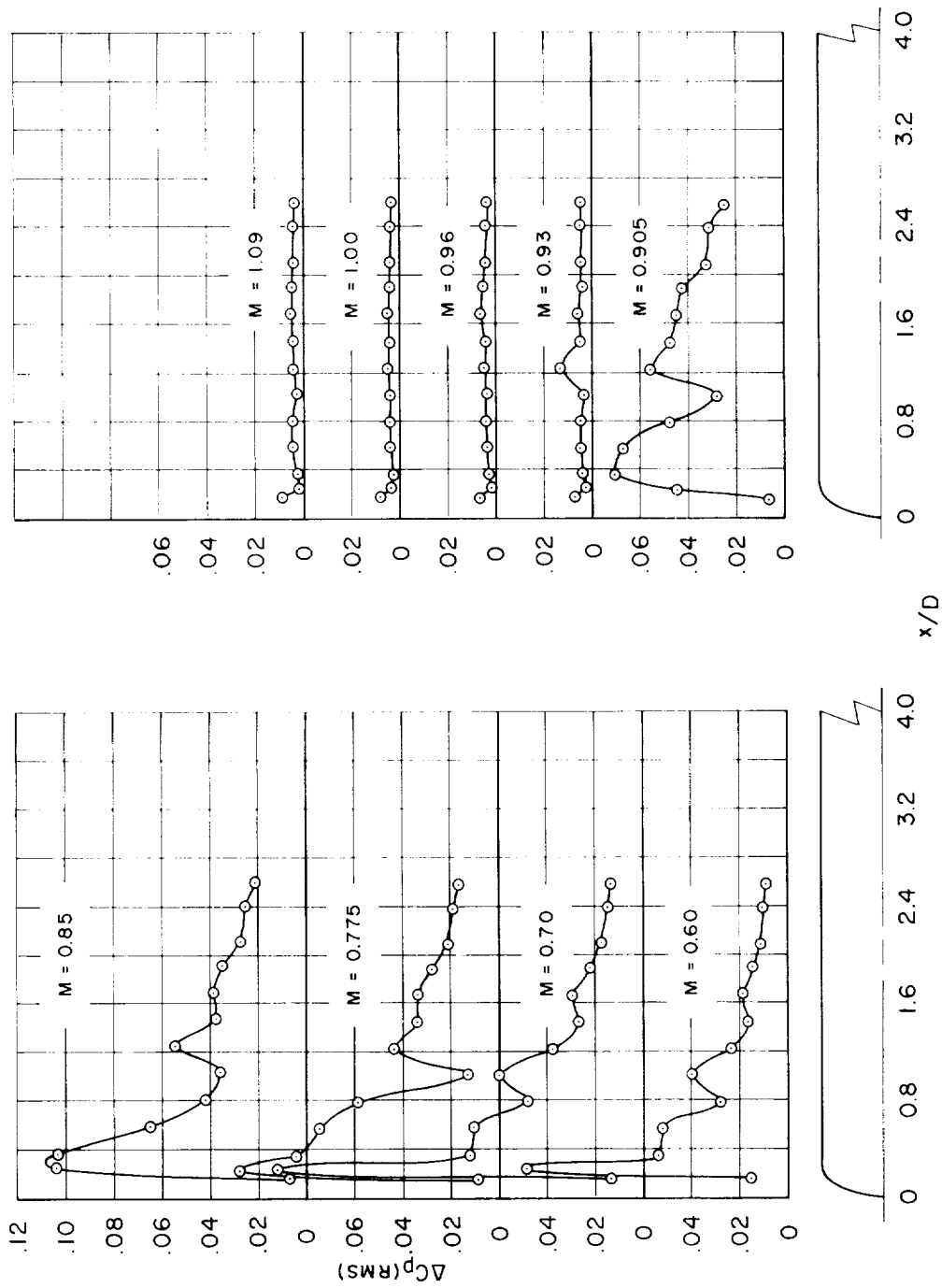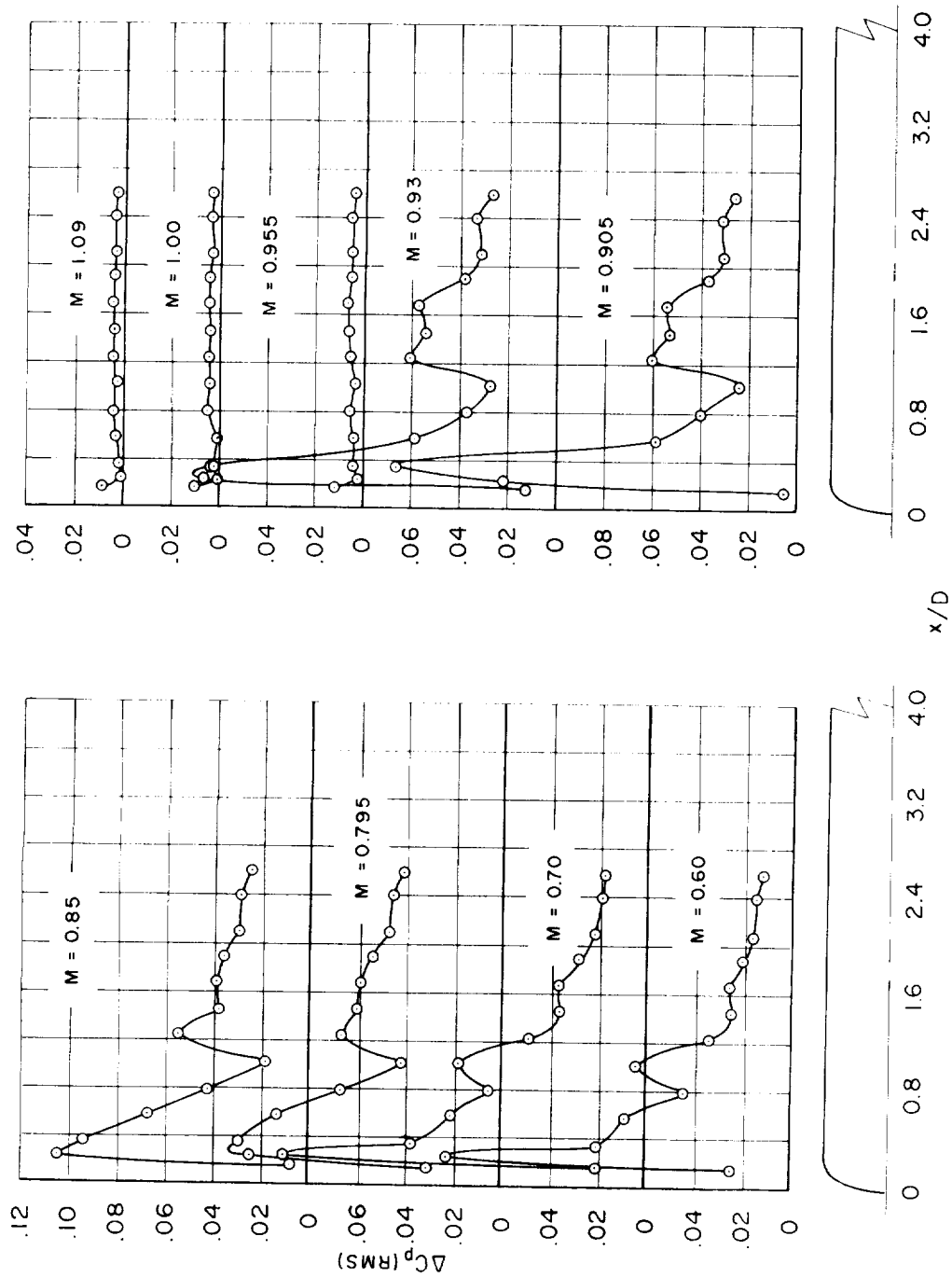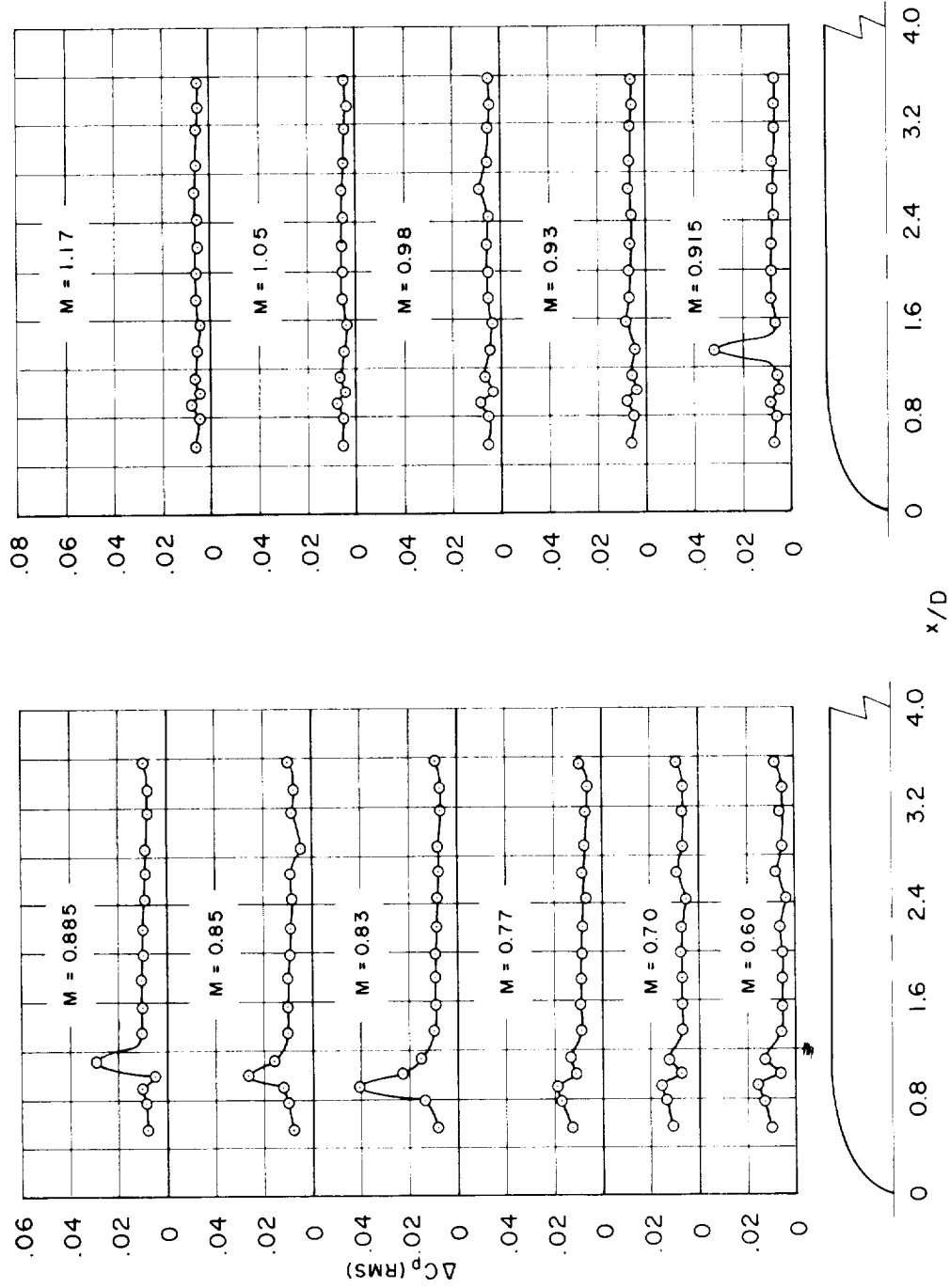
Figure 4.- Concluded.

(a) $\alpha = 4°$

Figure 5.- Longitudinal distributions of the pressure fluctuations on model II.

(b) $\alpha = 0°$

Figure 5.- Continued.

(c) $\alpha = 4°$
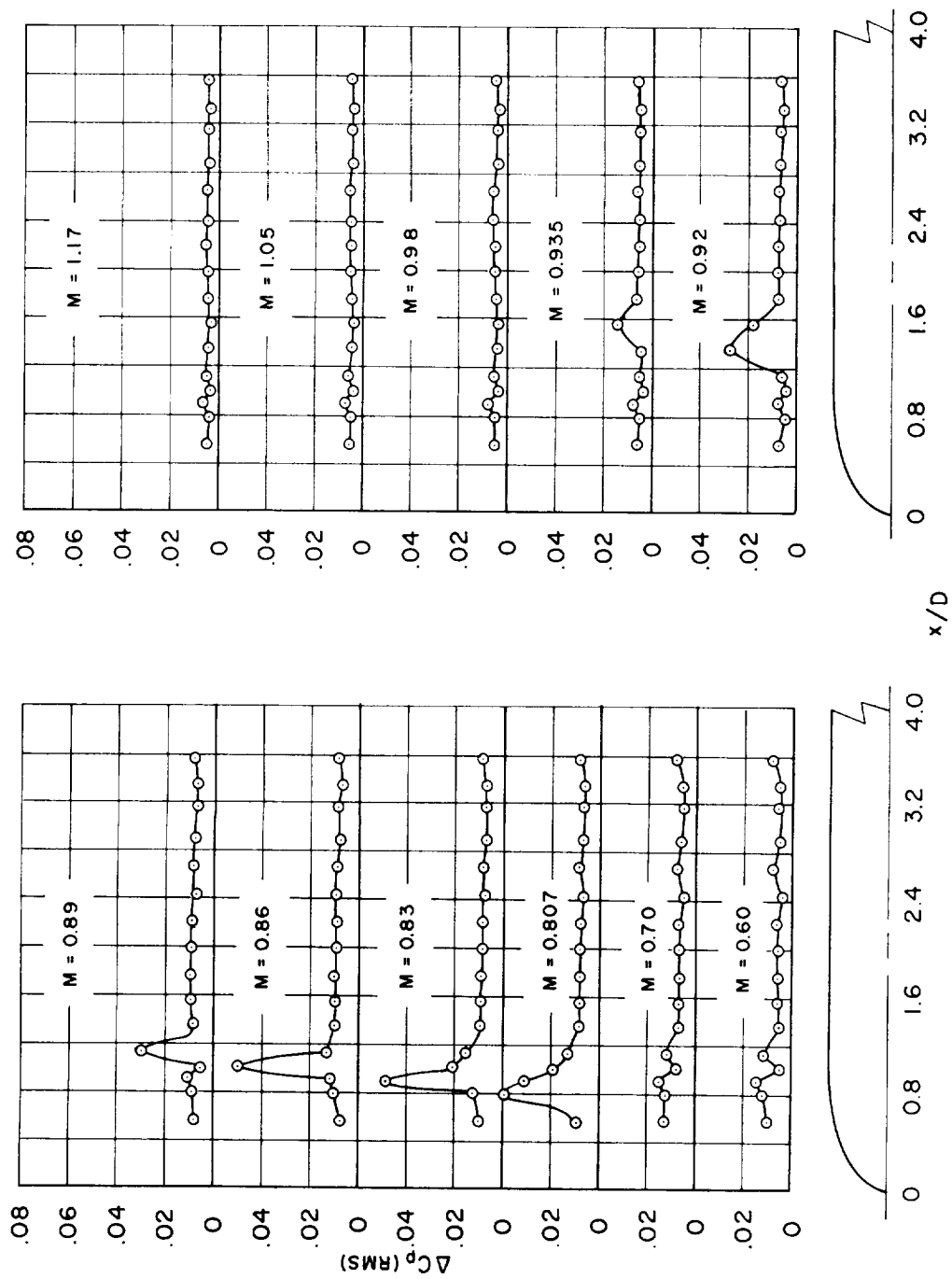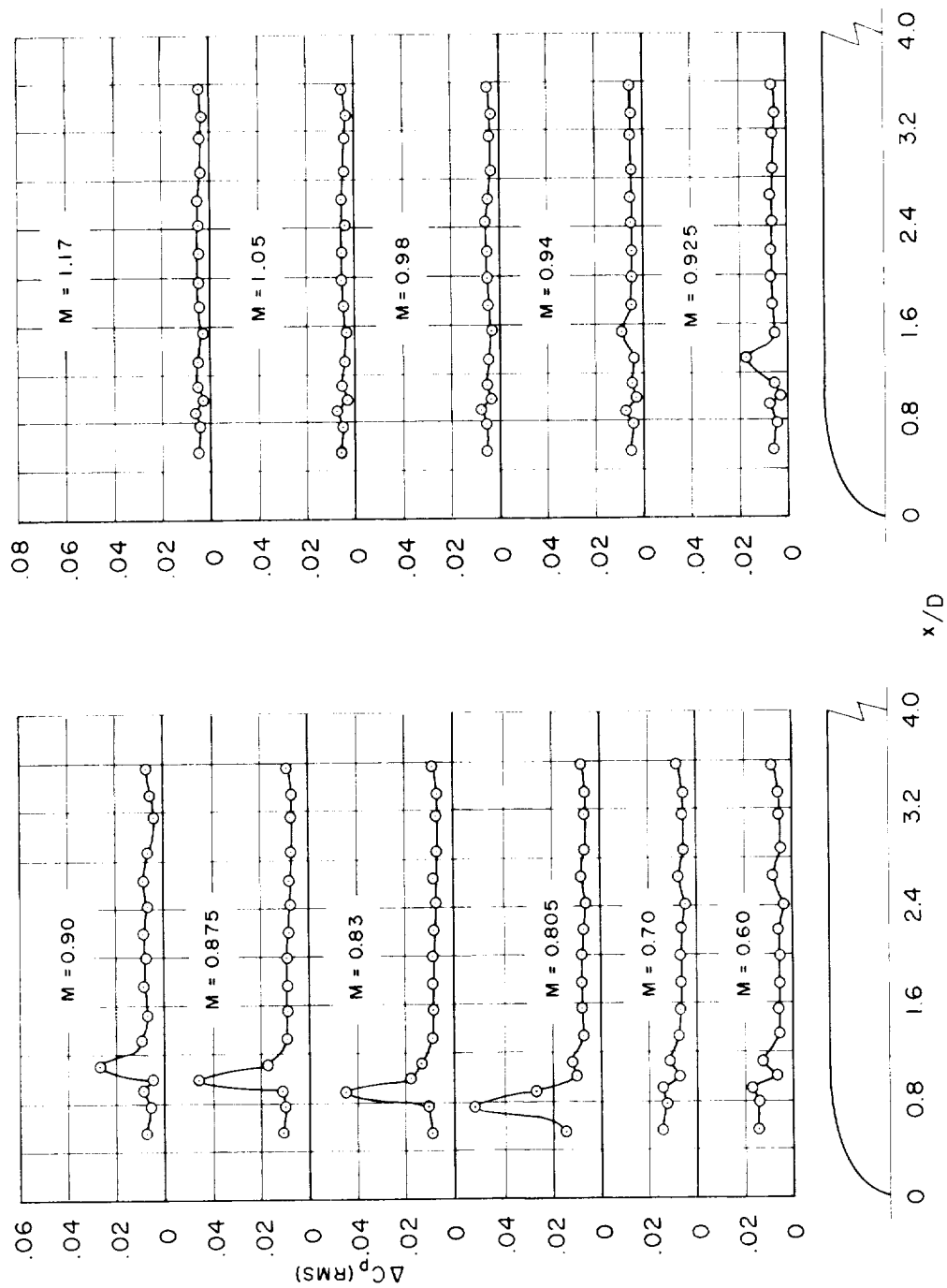
Figure 5.- Continued.
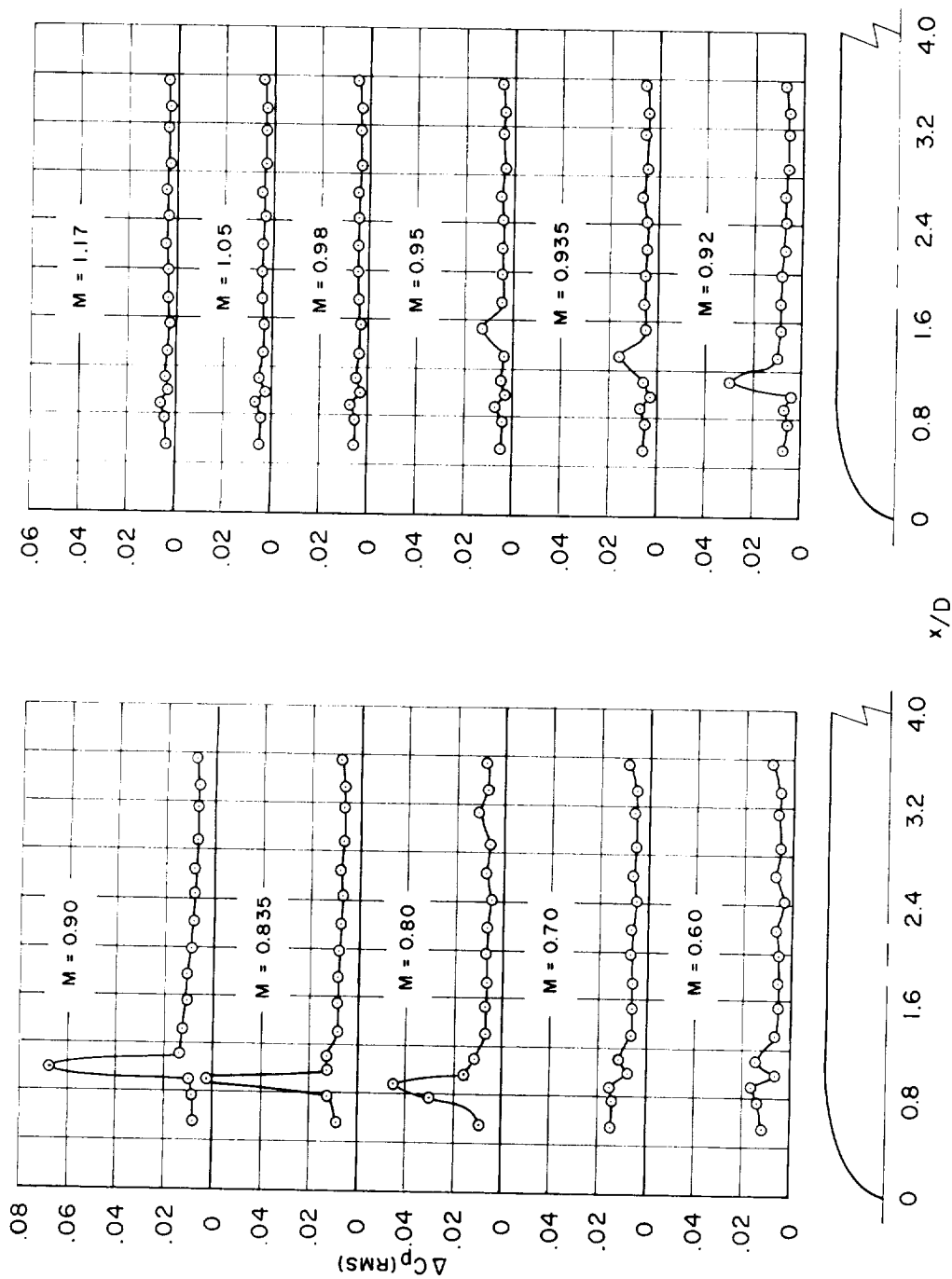
(d) α = 8°

Figure 5.- Concluded.
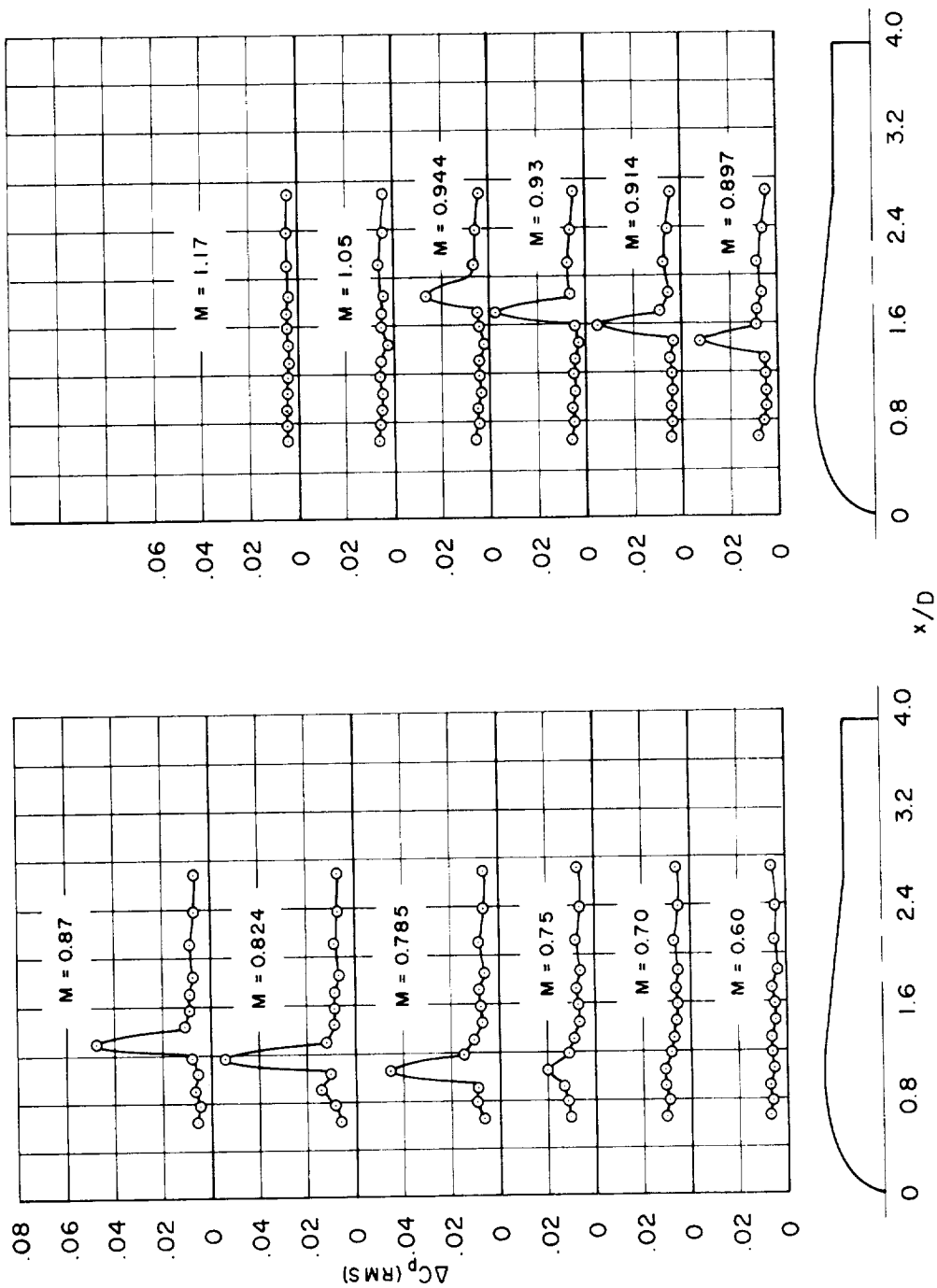
(a) $\alpha = -4^{\circ}$

Figure 6.- Longitudinal distributions of the pressure fluctuations on model III.

(b) $\alpha = 0°$

Figure 6.- Continued.

.08
.06
.04
.02
0

M = 1.17

.02
0

M = 1.05

.02
0

M = 0.97

.02
0

M = 0.965

.04
.02
0

M = 0.958

.04
.02
0

M = 0.95

.08
.06
.04
.02
0

M = 0.933

.04
.02
0

M = 0.89

.04
.02
0

M = 0.792

.02
0

M = 0.75

.02
0

M = 0.70

.02
0

M = 0.60

ΔC_p(RMS)

0   0.8   1.6   2.4   3.2   4.0

0   0.8   1.6   2.4   3.2   4.0

x/D

(c) $\alpha = 4^\circ$

Figure 5.- Continued.

A
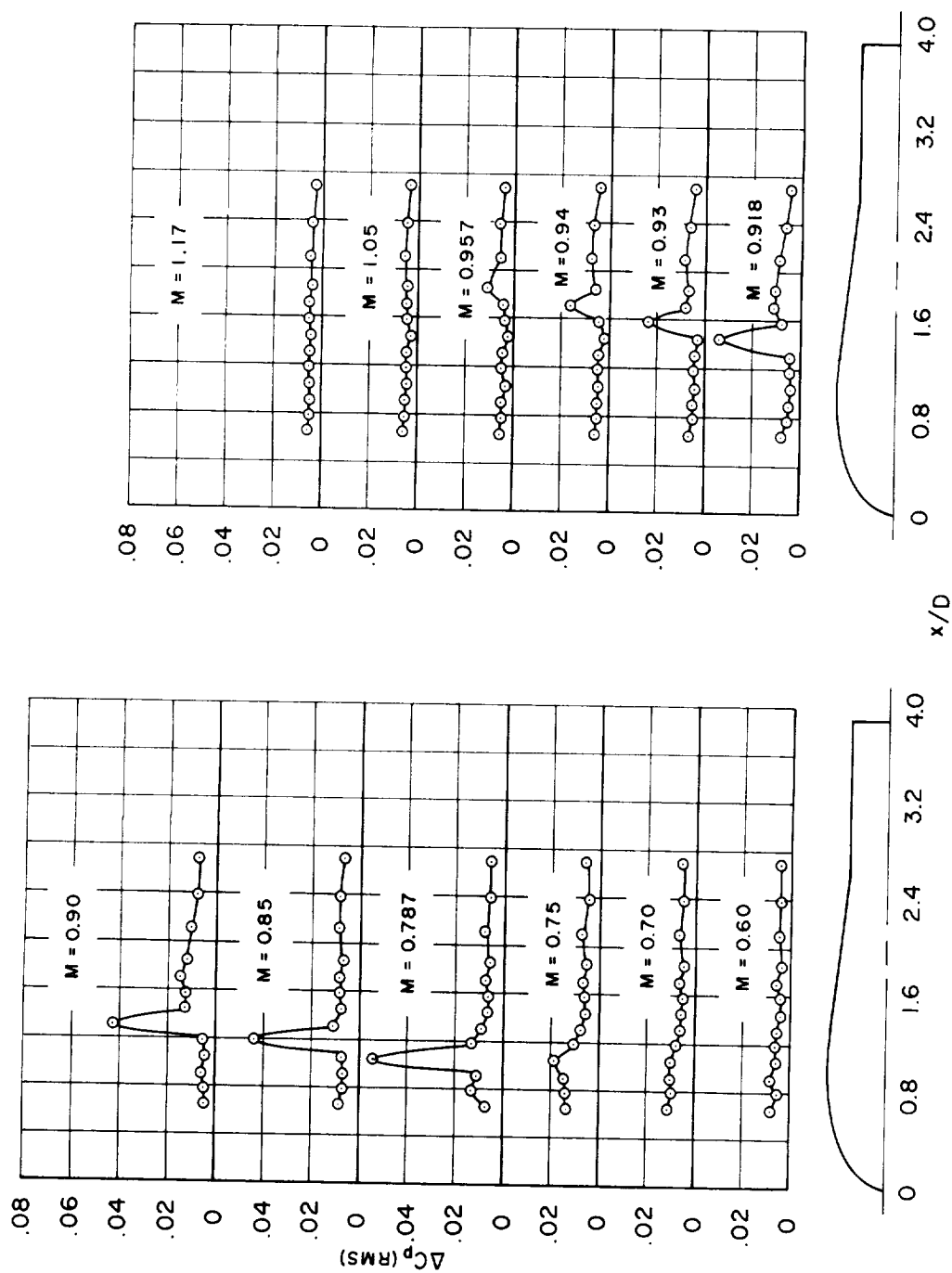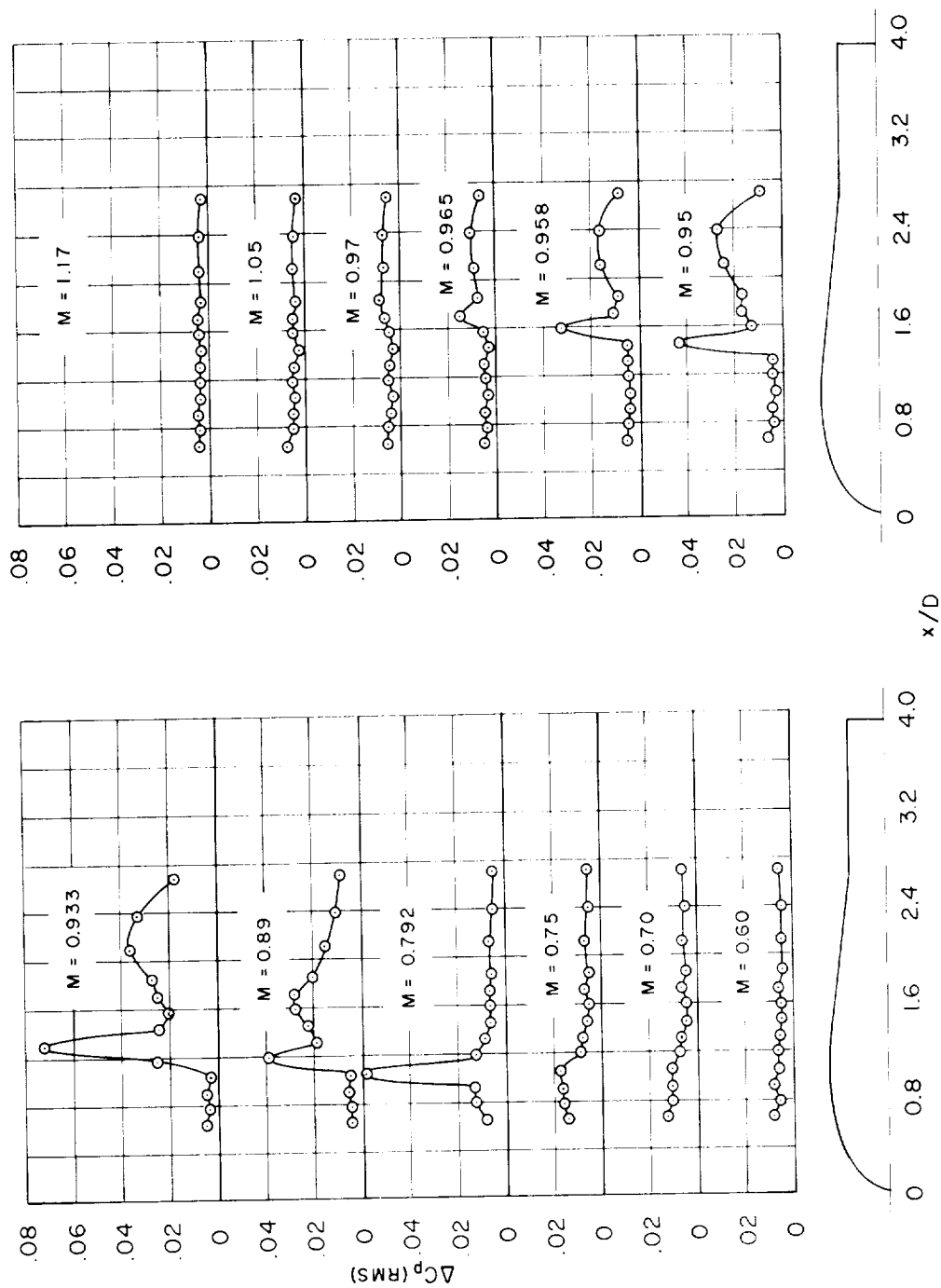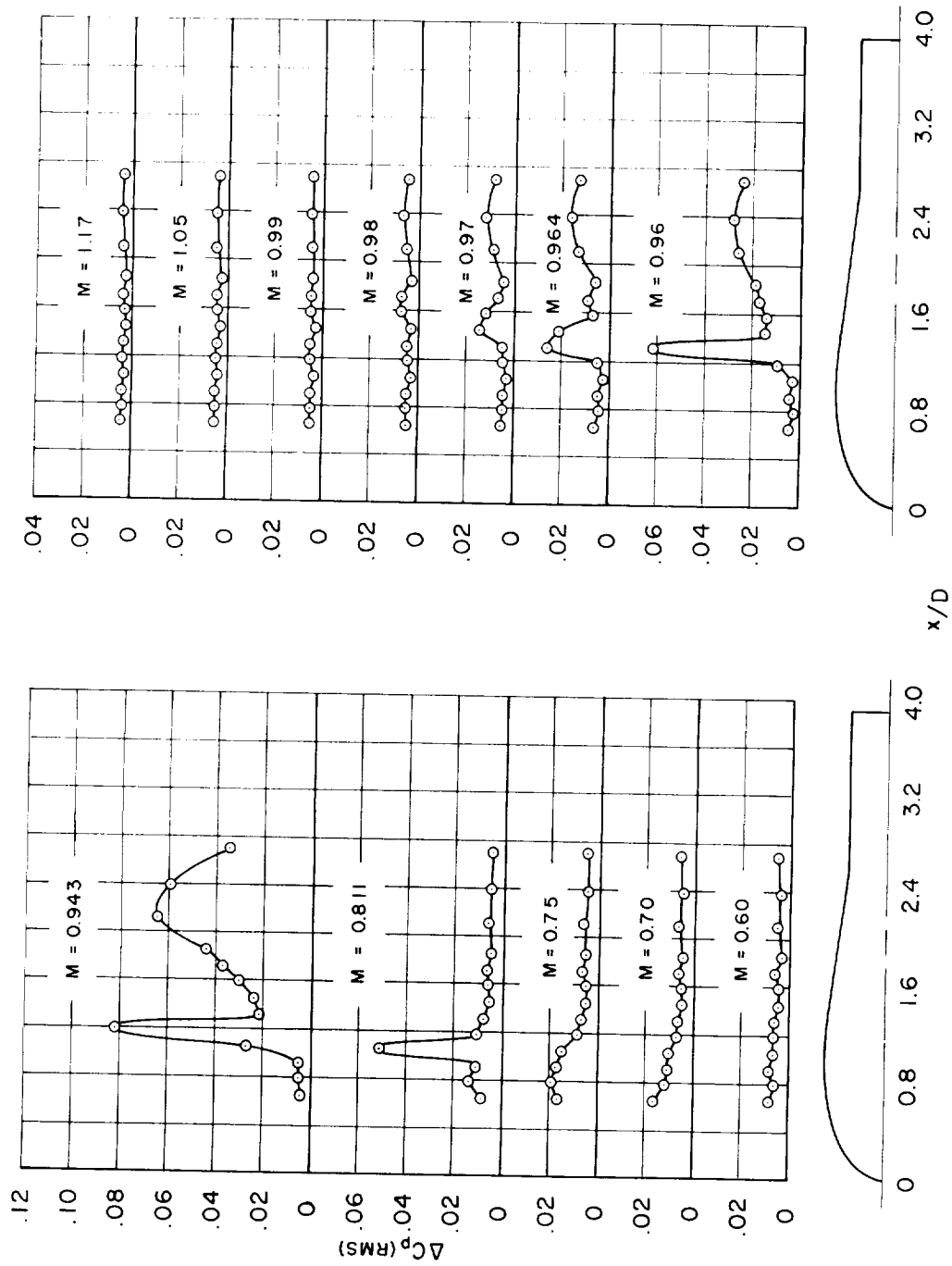
(d) $\alpha = 8°$
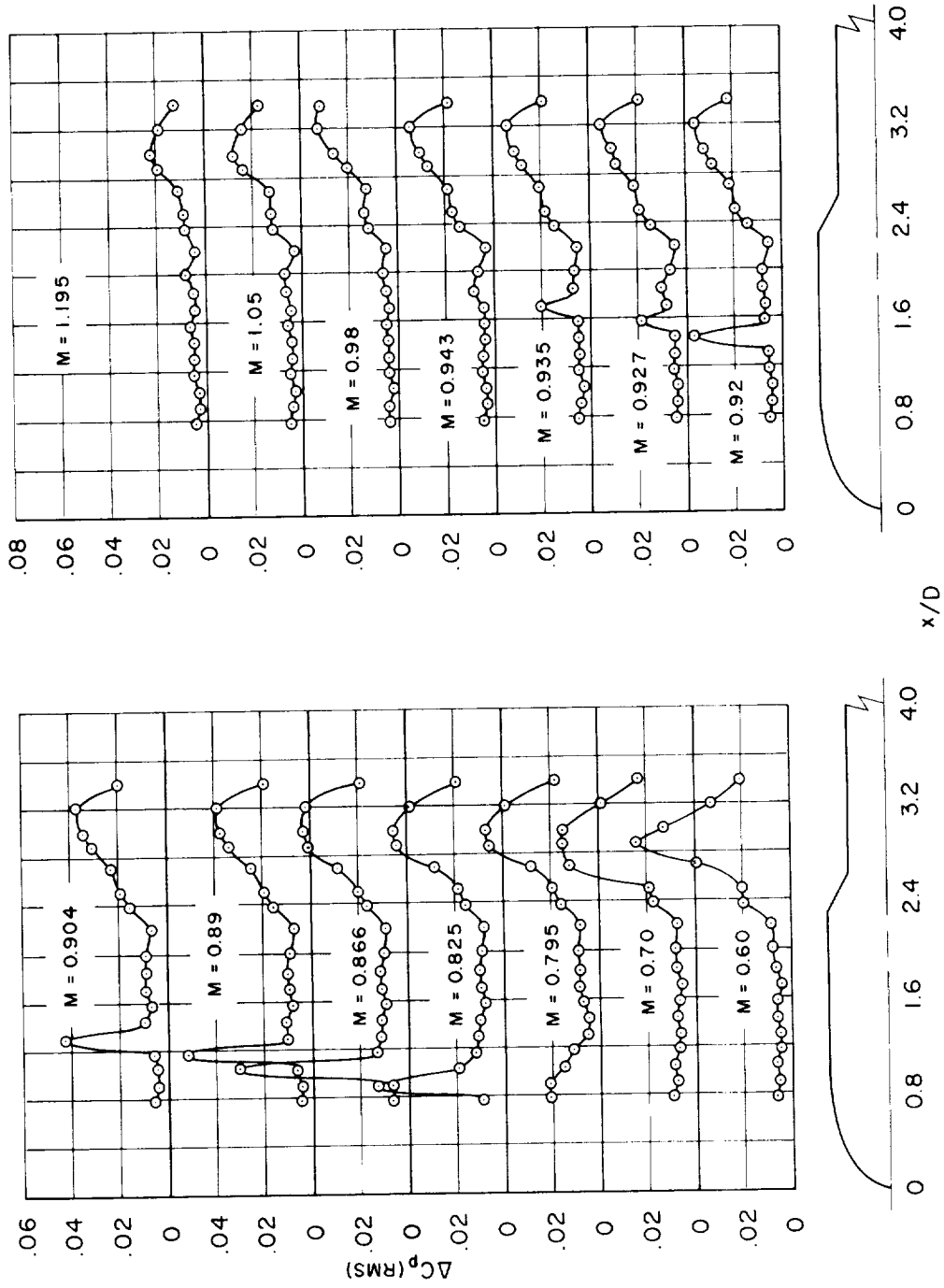
Figure 6.- Concluded.

Figure 7.- Longitudinal distributions of the pressure fluctuations on model IV.

(a) $\alpha = -4°$
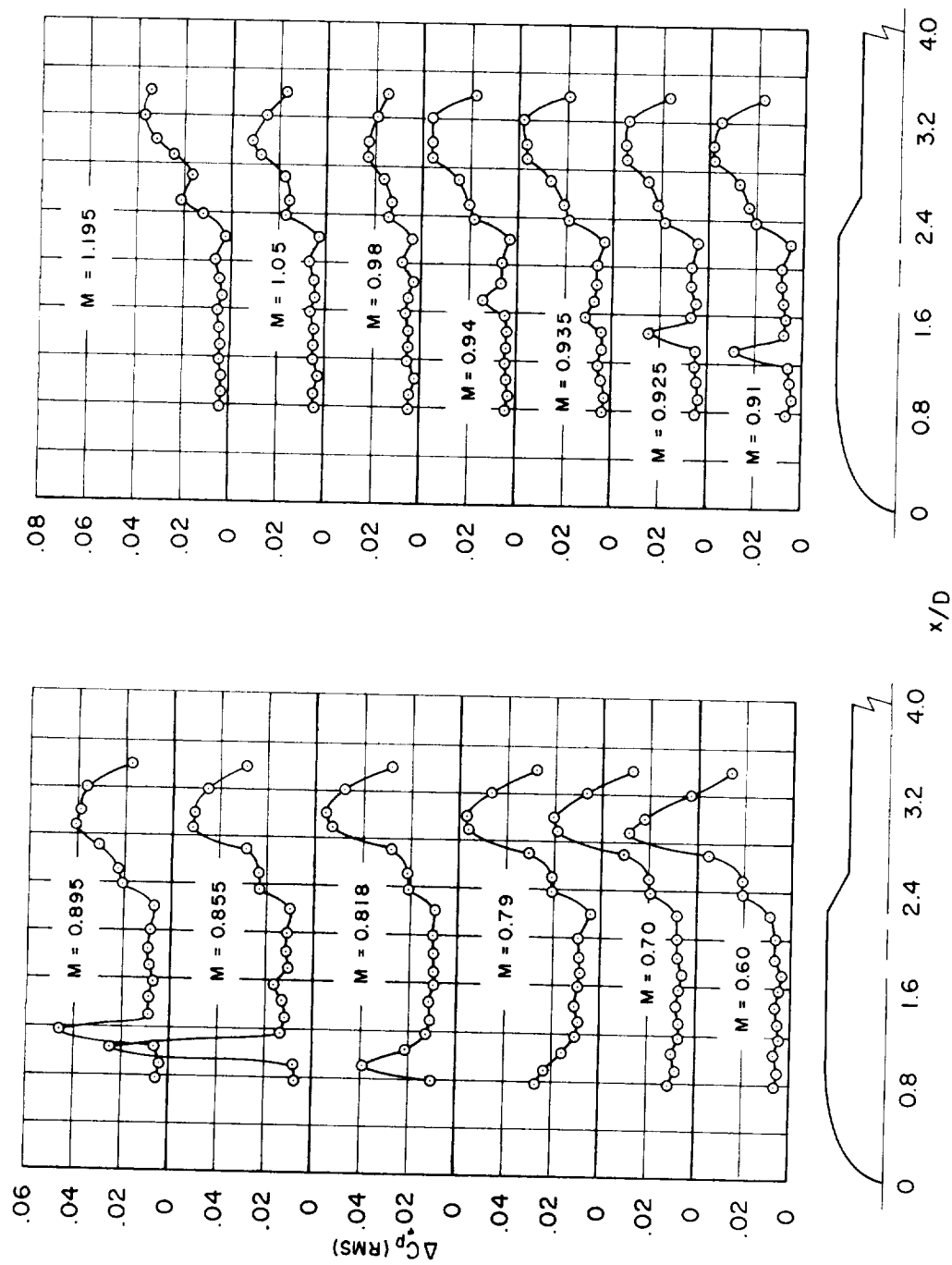
(b) $\alpha = 0°$

Figure 7.- Continued.
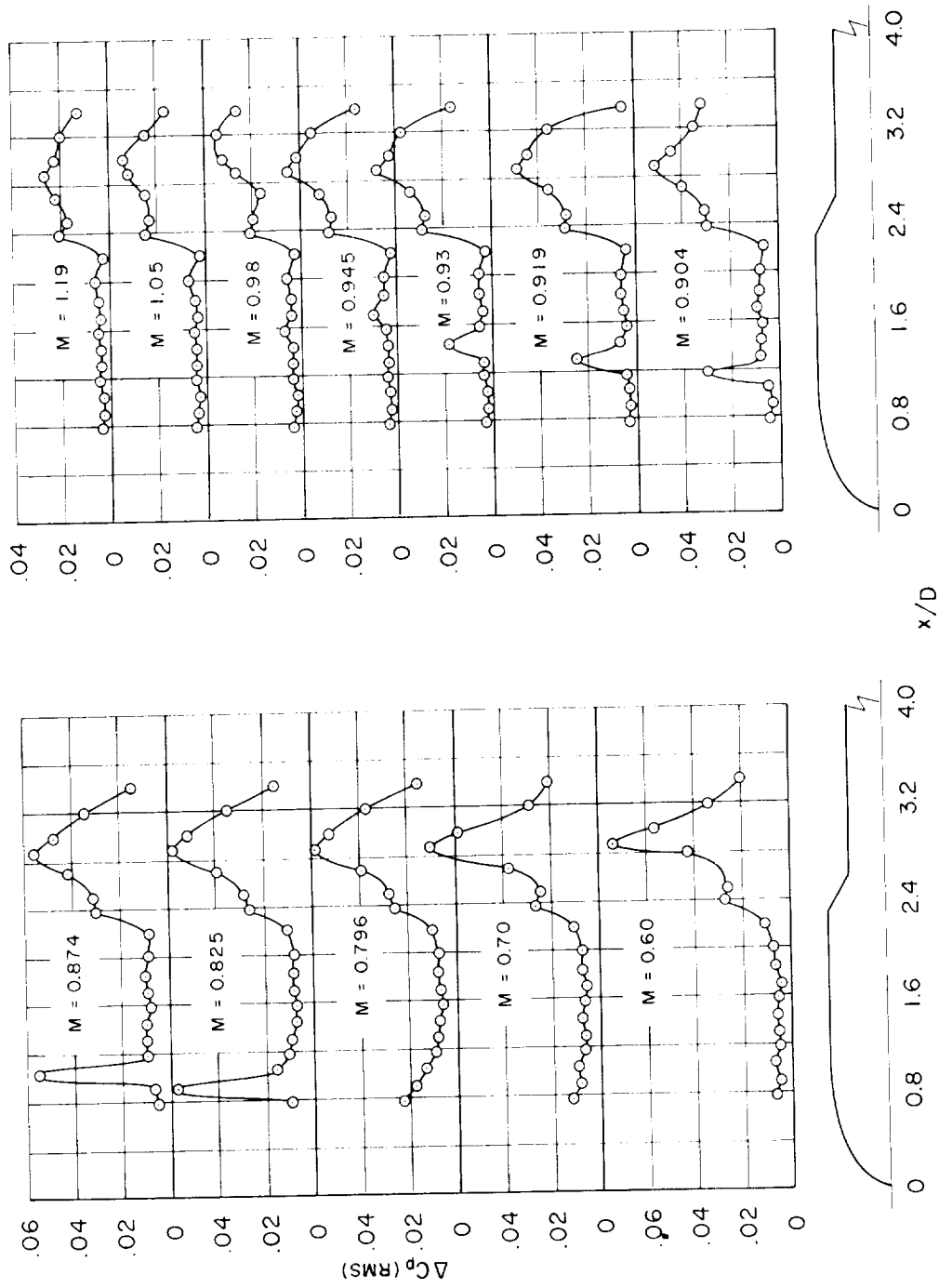
(c) $\alpha = 4°$

Figure 7.- Continued.
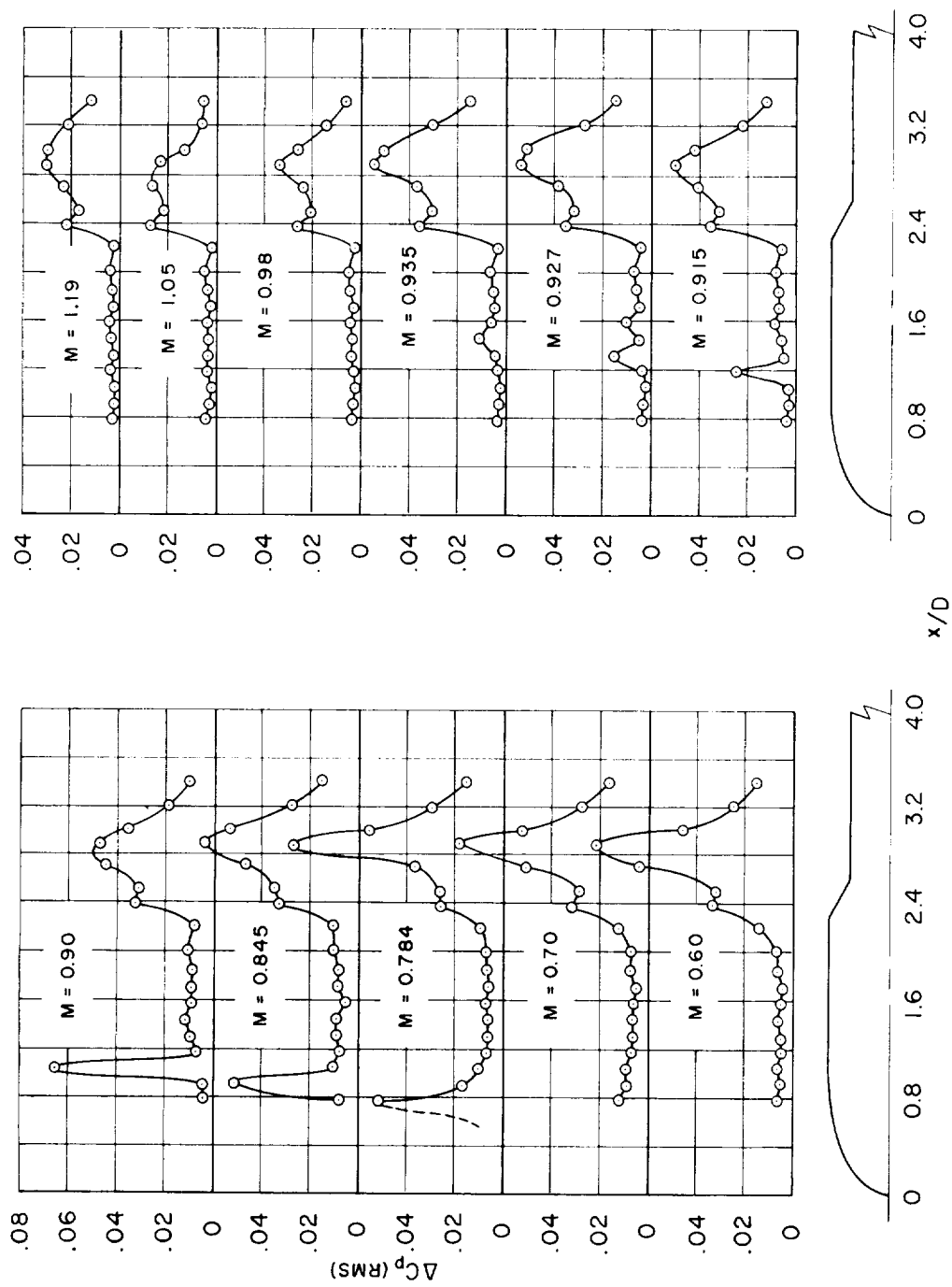
(d) $\alpha = 8°$

Figure 7.- Concluded.

34
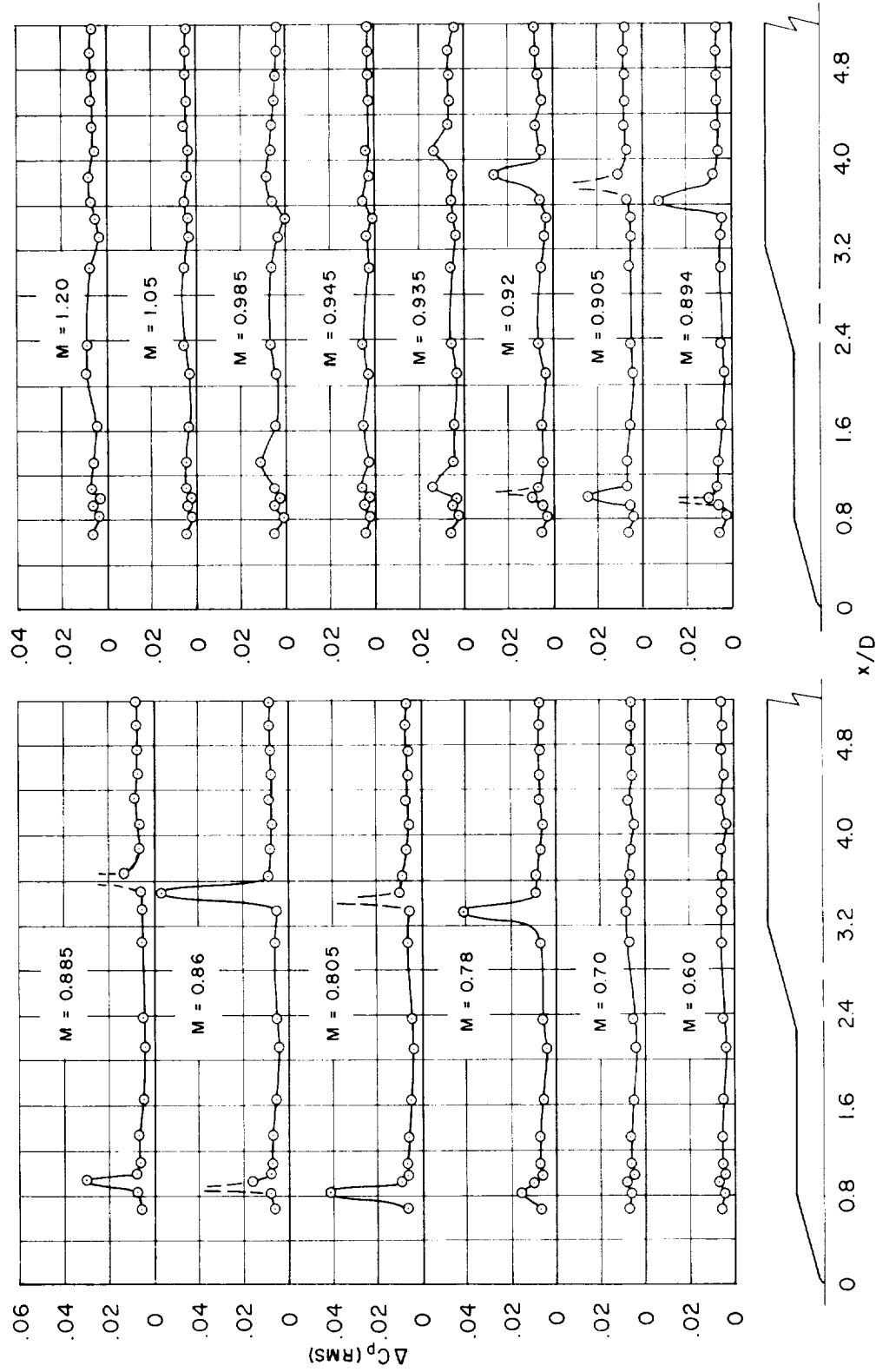
Figure 8.- Longitudinal distributions of the pressure fluctuations on model V.

(a) $\alpha = 4^\circ$

(b) $\alpha = 0°$
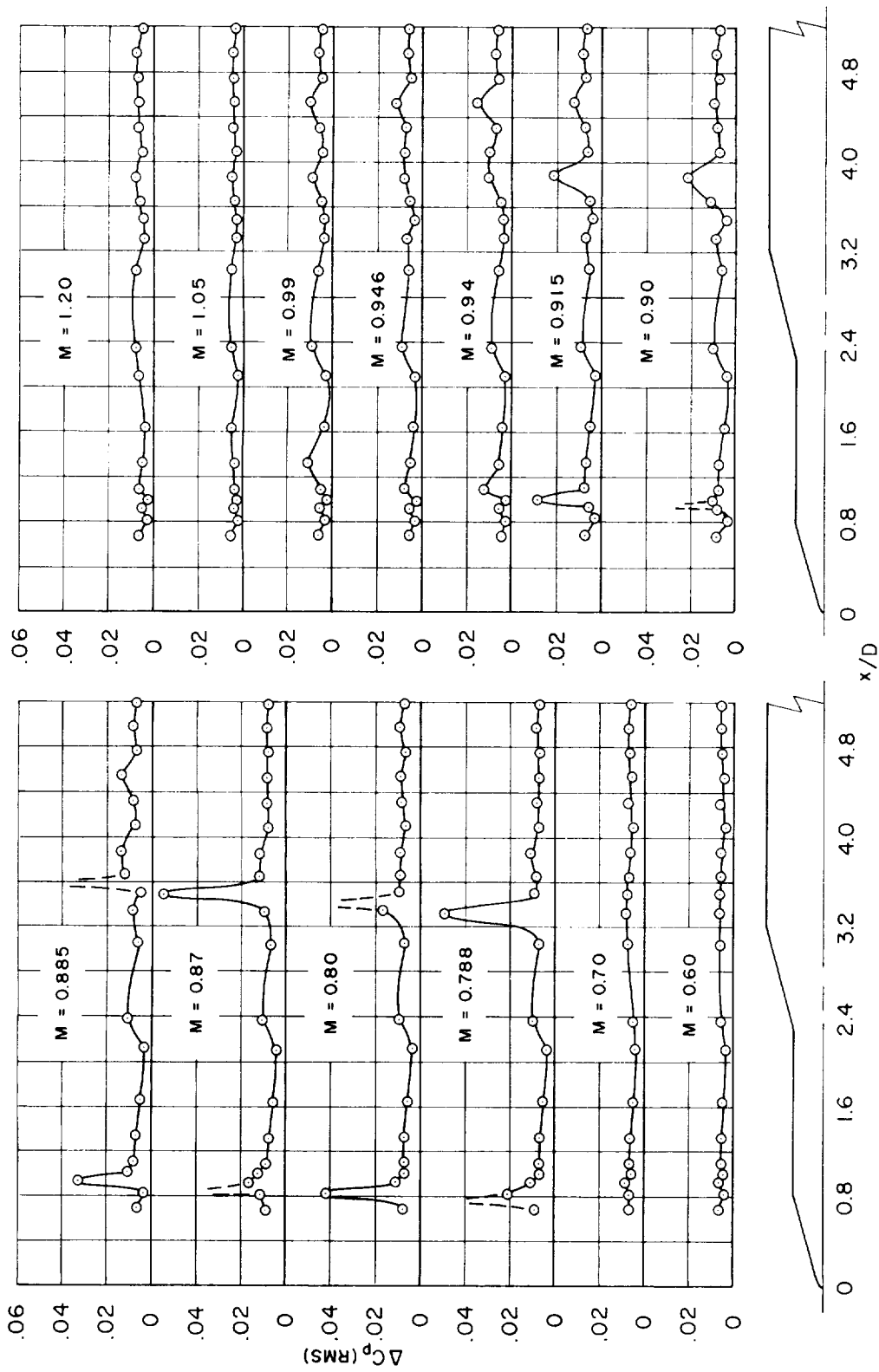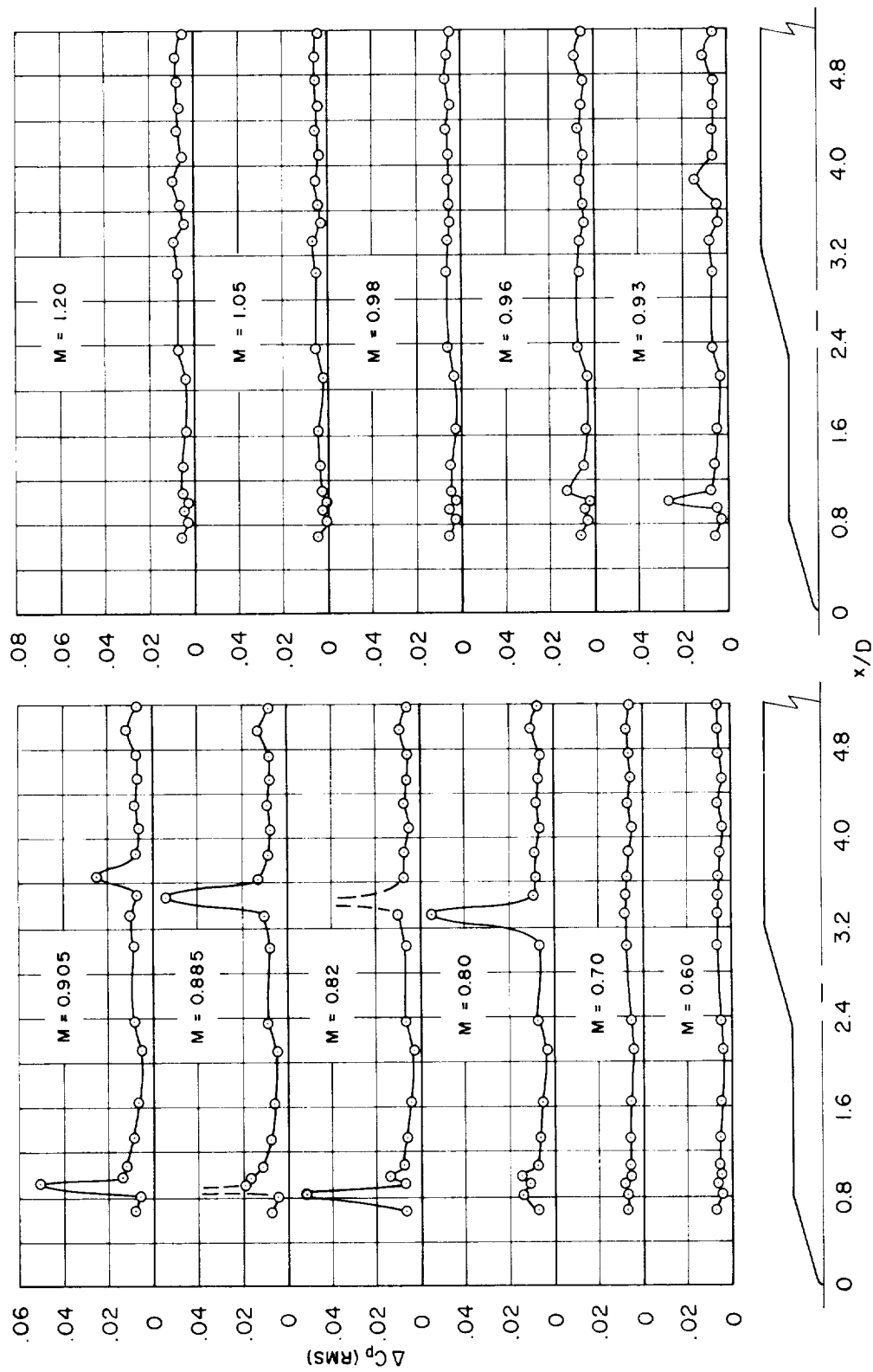
Figure 8.- Continued.

(c) $\alpha = 4°$

Figure 8.- Continued.

(d) $\alpha = 8^\circ$
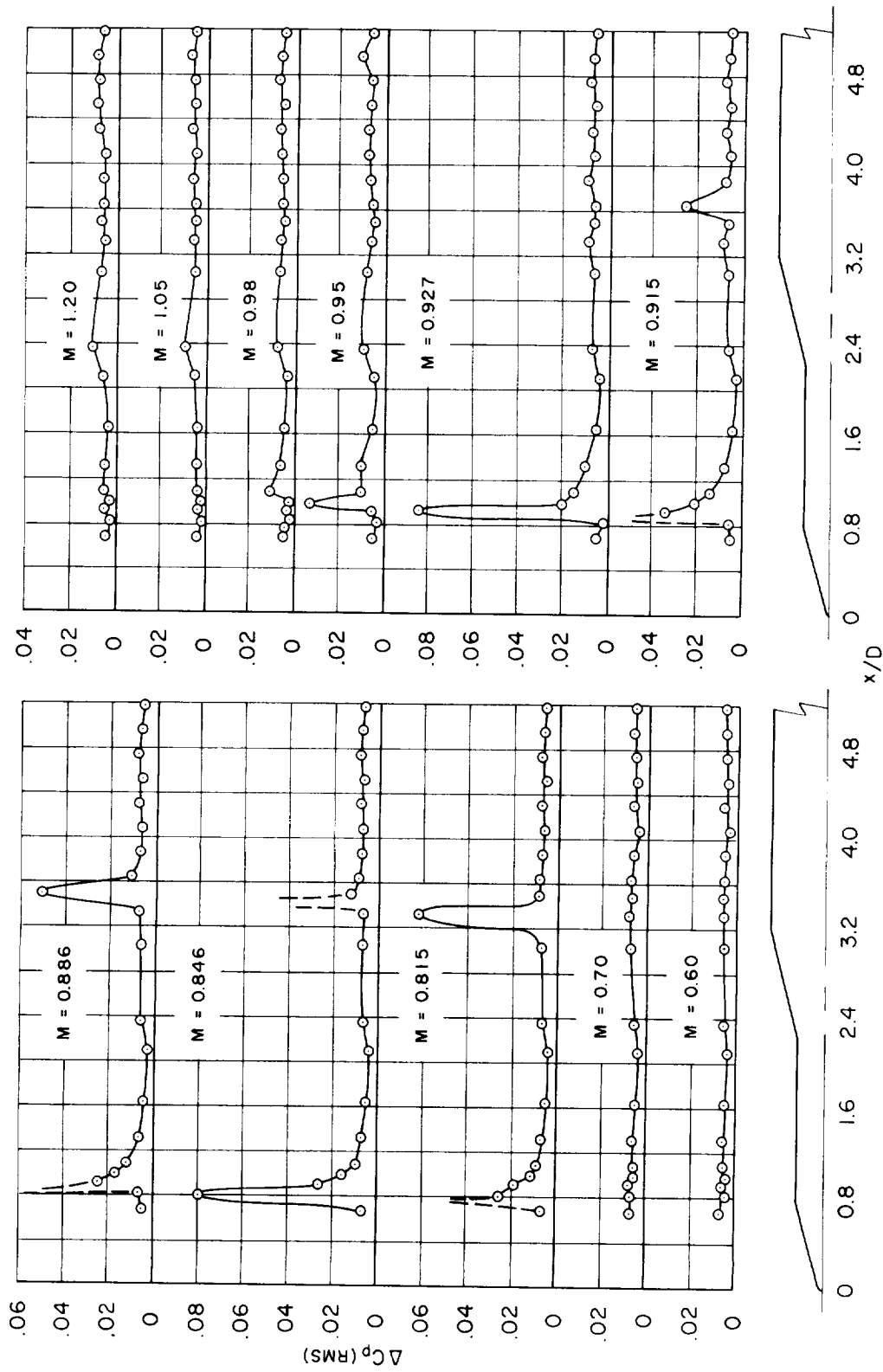
Figure 8.- Continued.
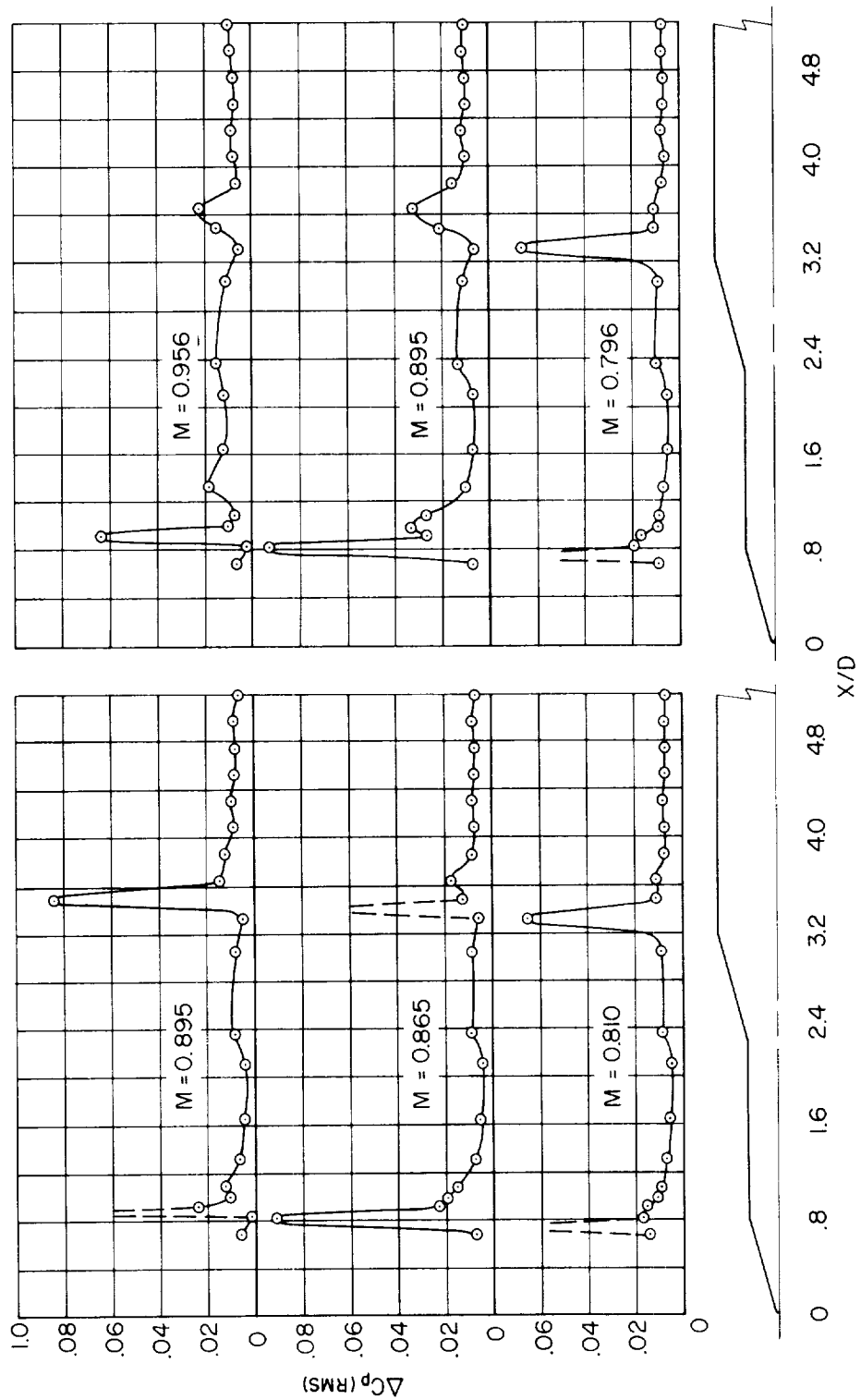
(e) $\alpha = 12^{\circ}$, 16°

Figure 8.- Concluded.

Model I, M = 0.85
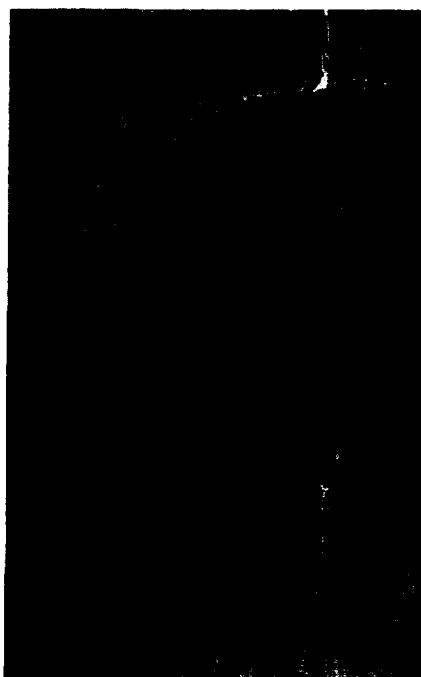
Hemispherical Nose, M = 0.80
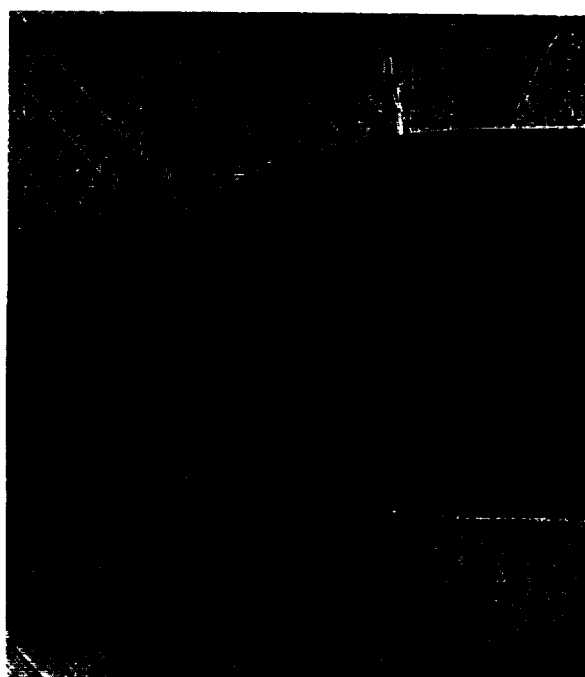
Model II, M = 0.80

Figure 9.- Shadowgraph pictures illustrating the effect of ellipsoidal nose bluntness on the flow at $\alpha = 0°$.
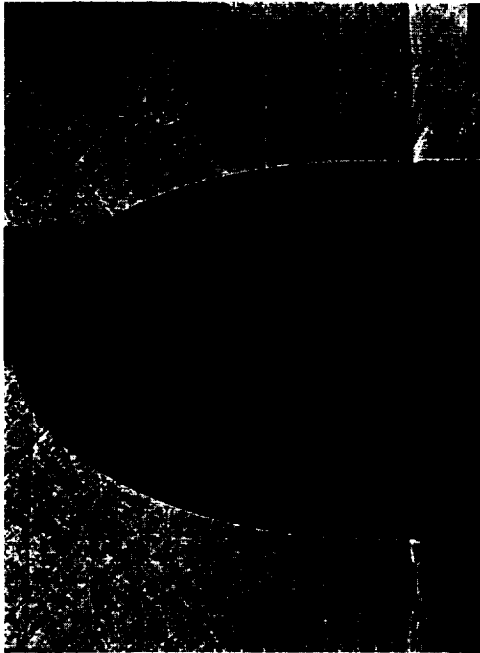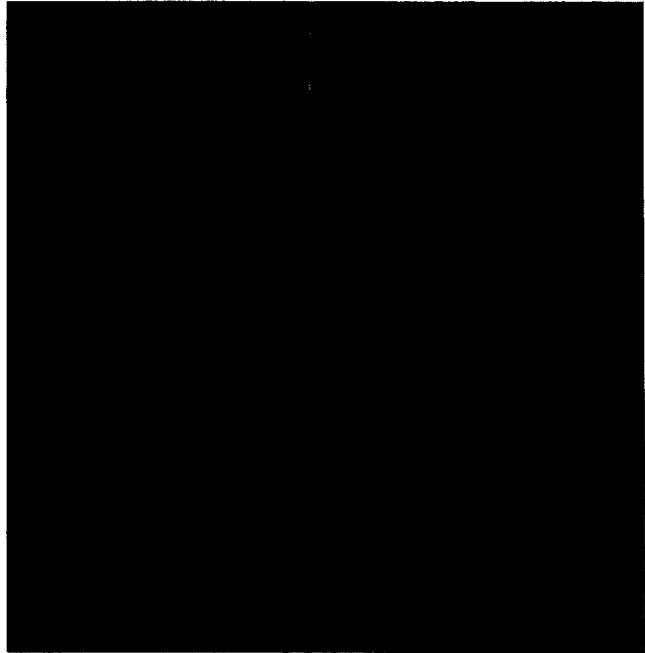
Model II, M = 0.90   Model III, M = 0.90
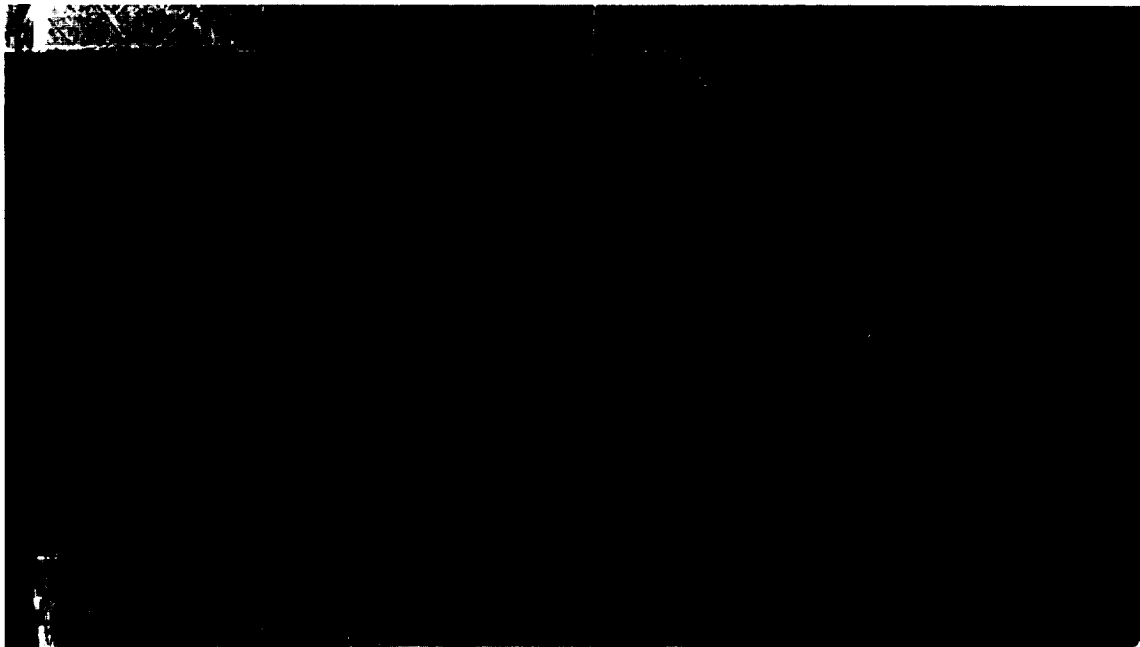
Model IV, M = 0.895

(a) $\alpha = 0^{\circ}$

Figure 10.- Shadowgraph pictures showing the effect of body convergence on the flow.

A
5
5
5
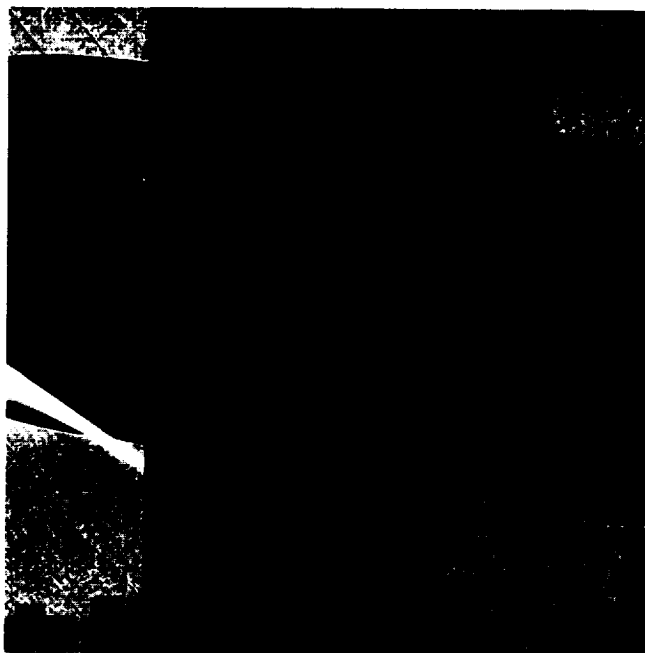
Model II, M = 0.90

Model III, M = 0.943
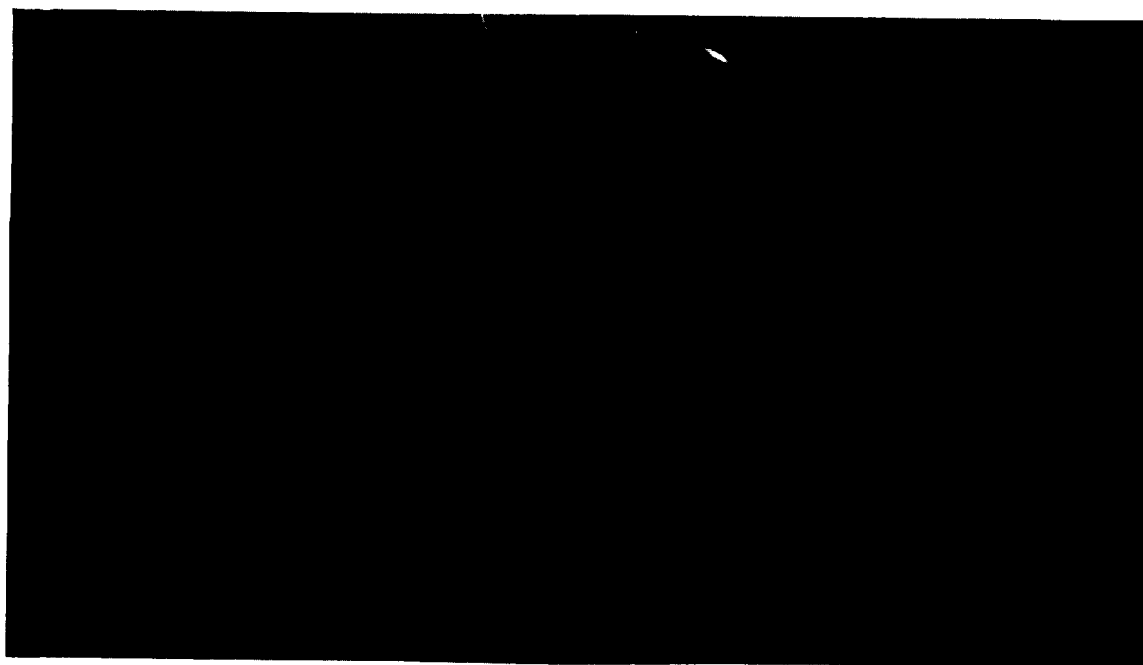
Model IV, M = 1.19

(b) $\alpha = 8^{\circ}$

Figure 10.- Concluded.
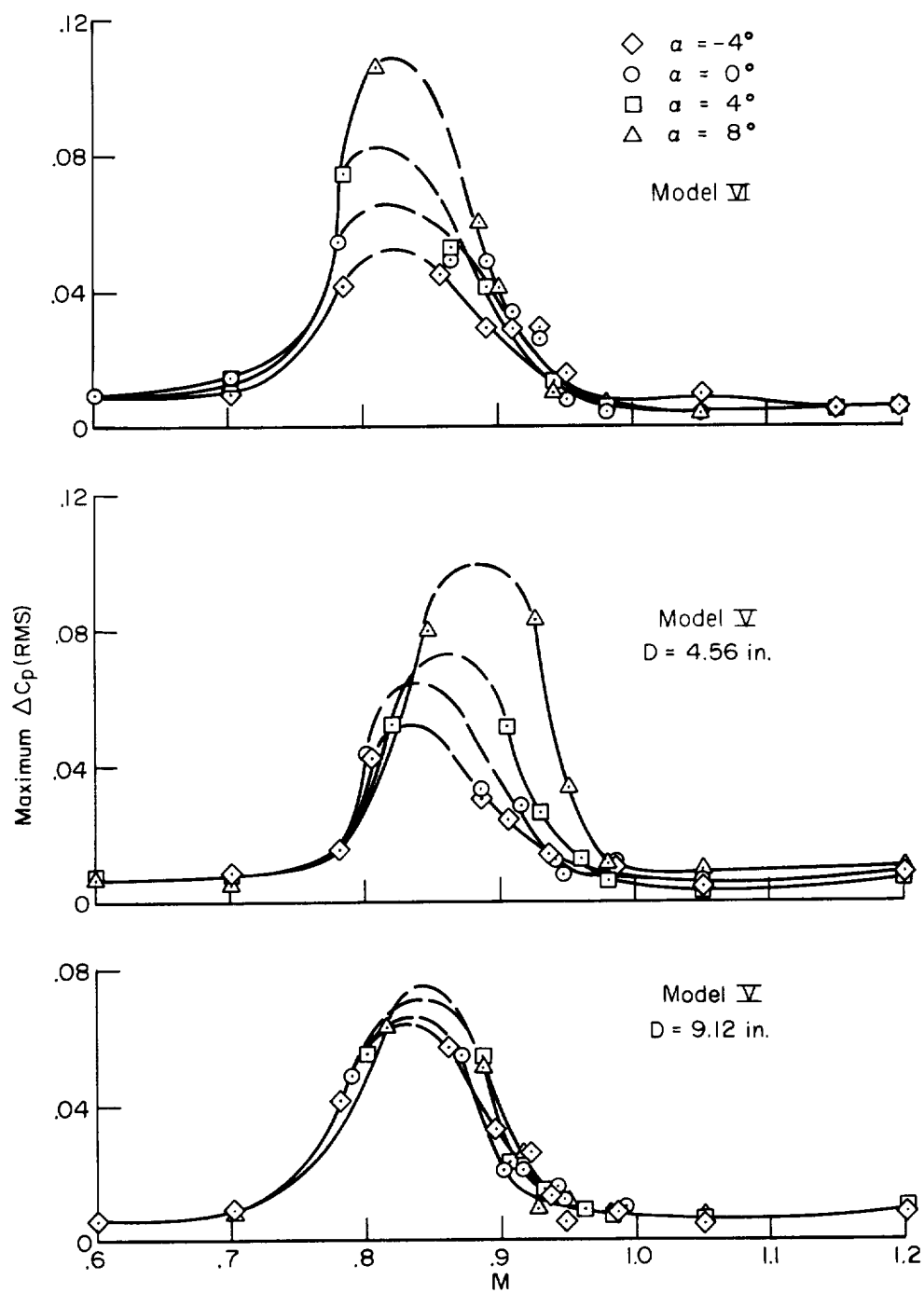
(a) Effect of diameter of similar model sections.

Figure 11.- The variation with Mach number of the maximum pressure
fluctuations measured on the cylindrical sections of models V
and VI.
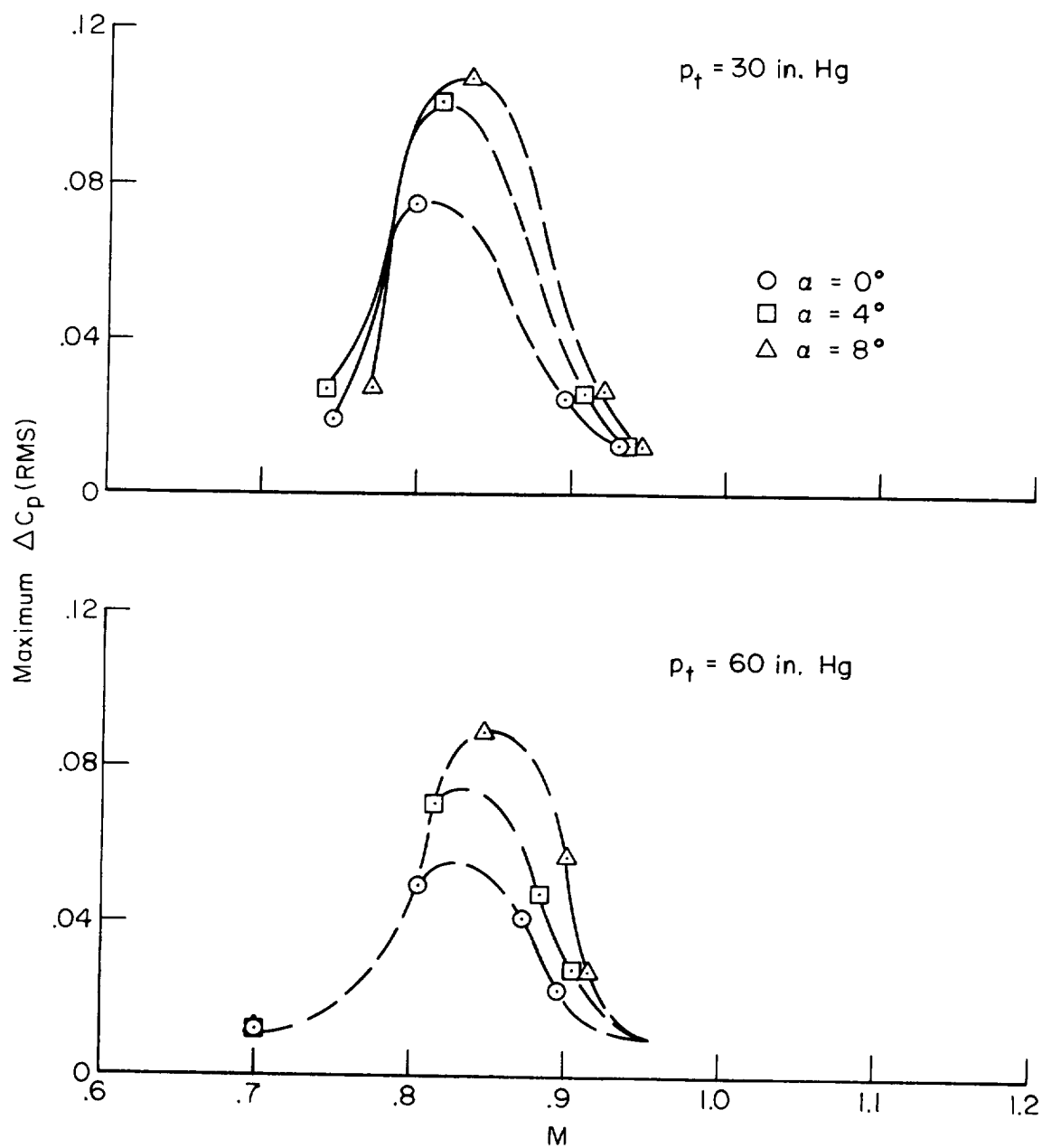
(b) Effect of stagnation pressure from tests of model VI in Ames 11-Foot Transonic Wind Tunnel.

Figure 11.- Concluded.
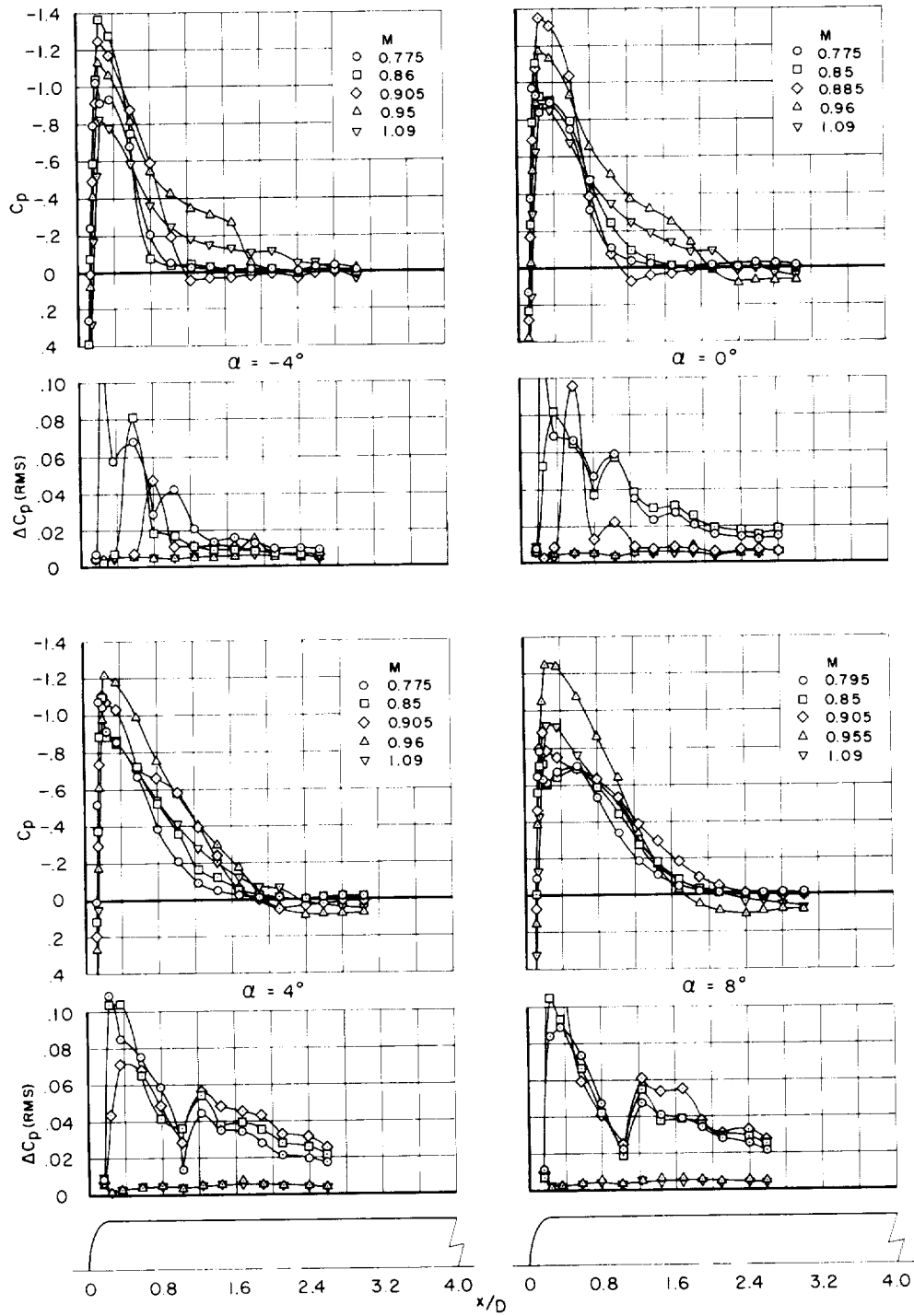
(a) Model I.

Figure 12.- Pressure fluctuations and time-average static-pressure distributions on the models.
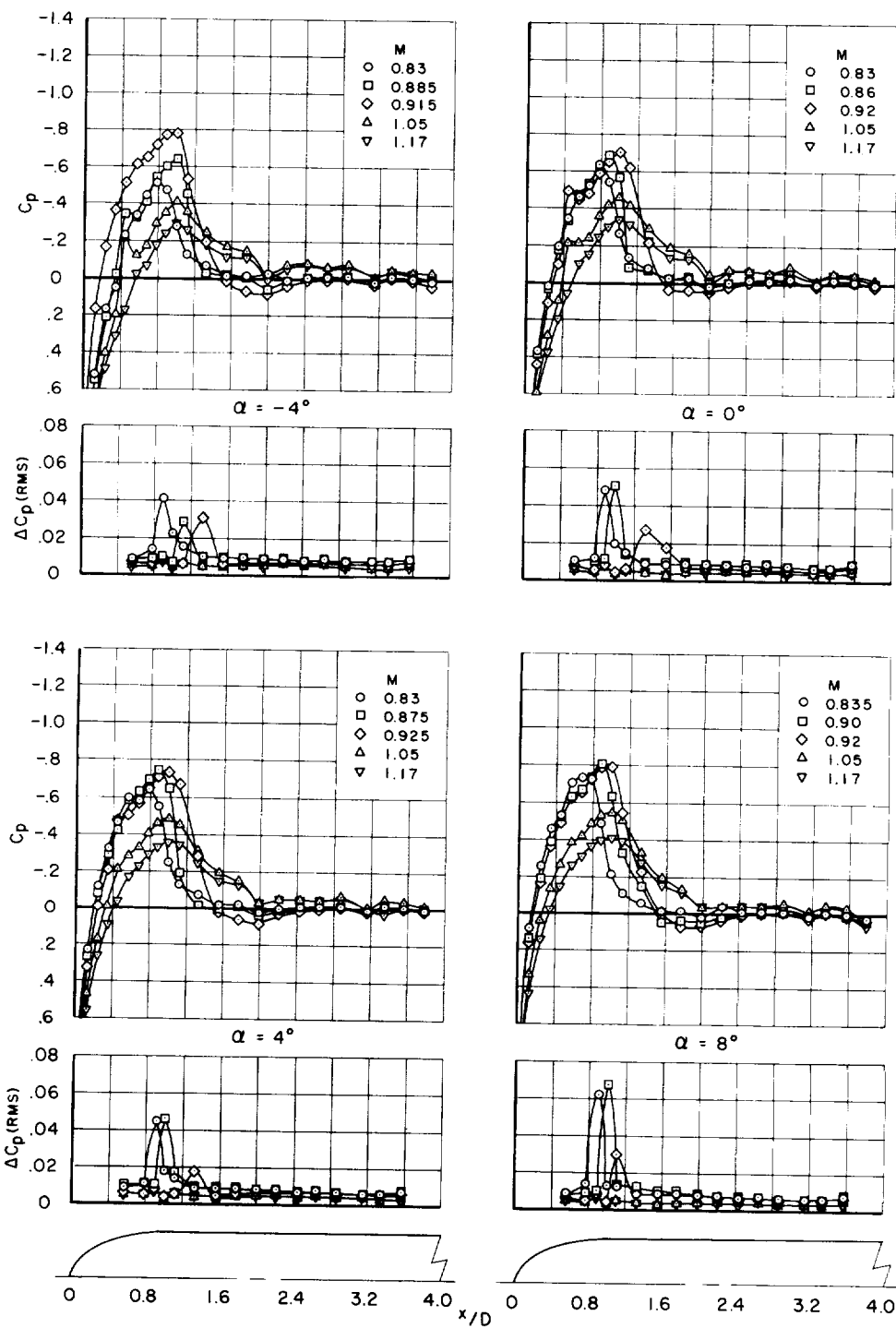
(b) Model II.

Figure 12.- Continued.
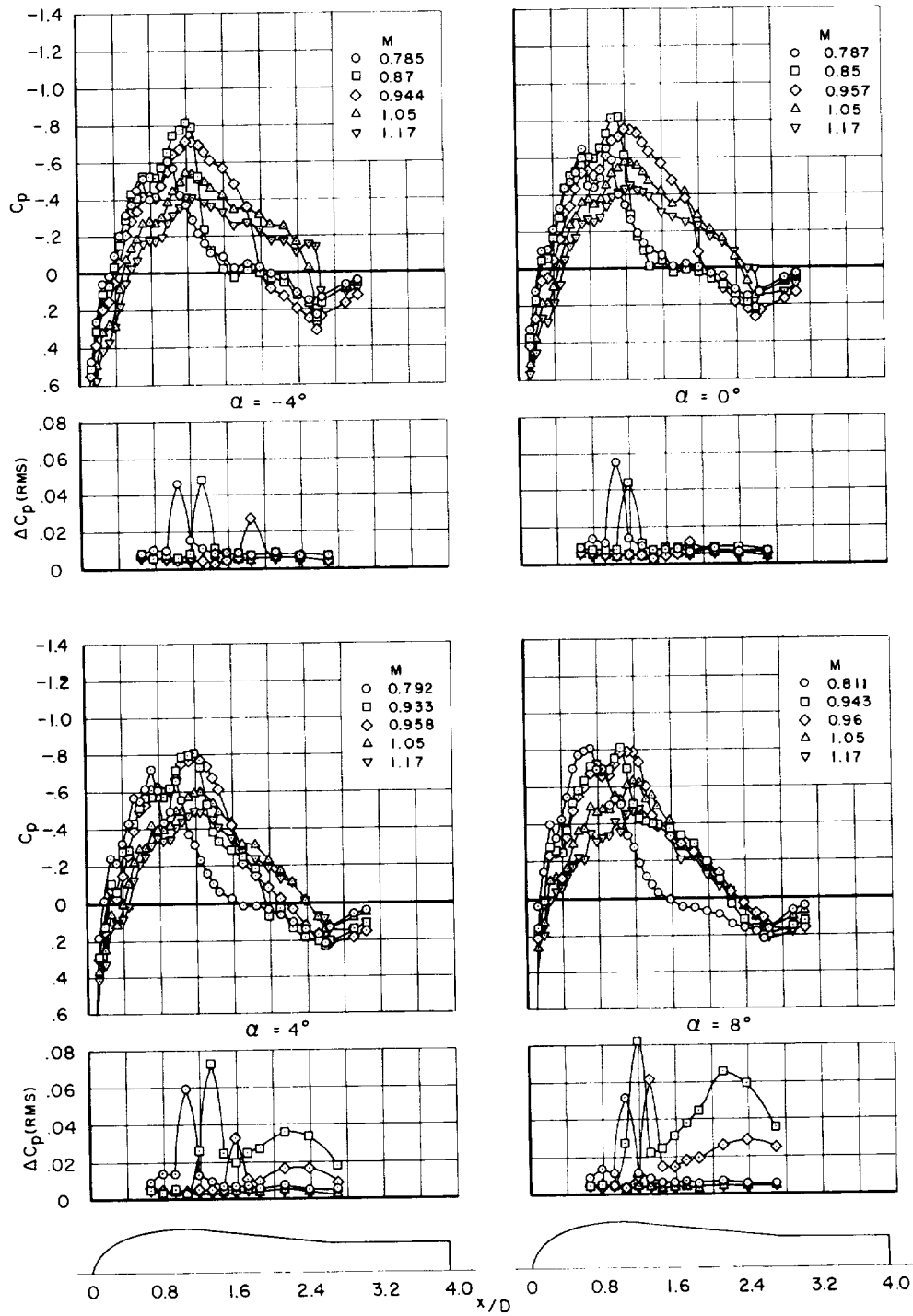
(c) Model III.

Figure 12.- Continued.
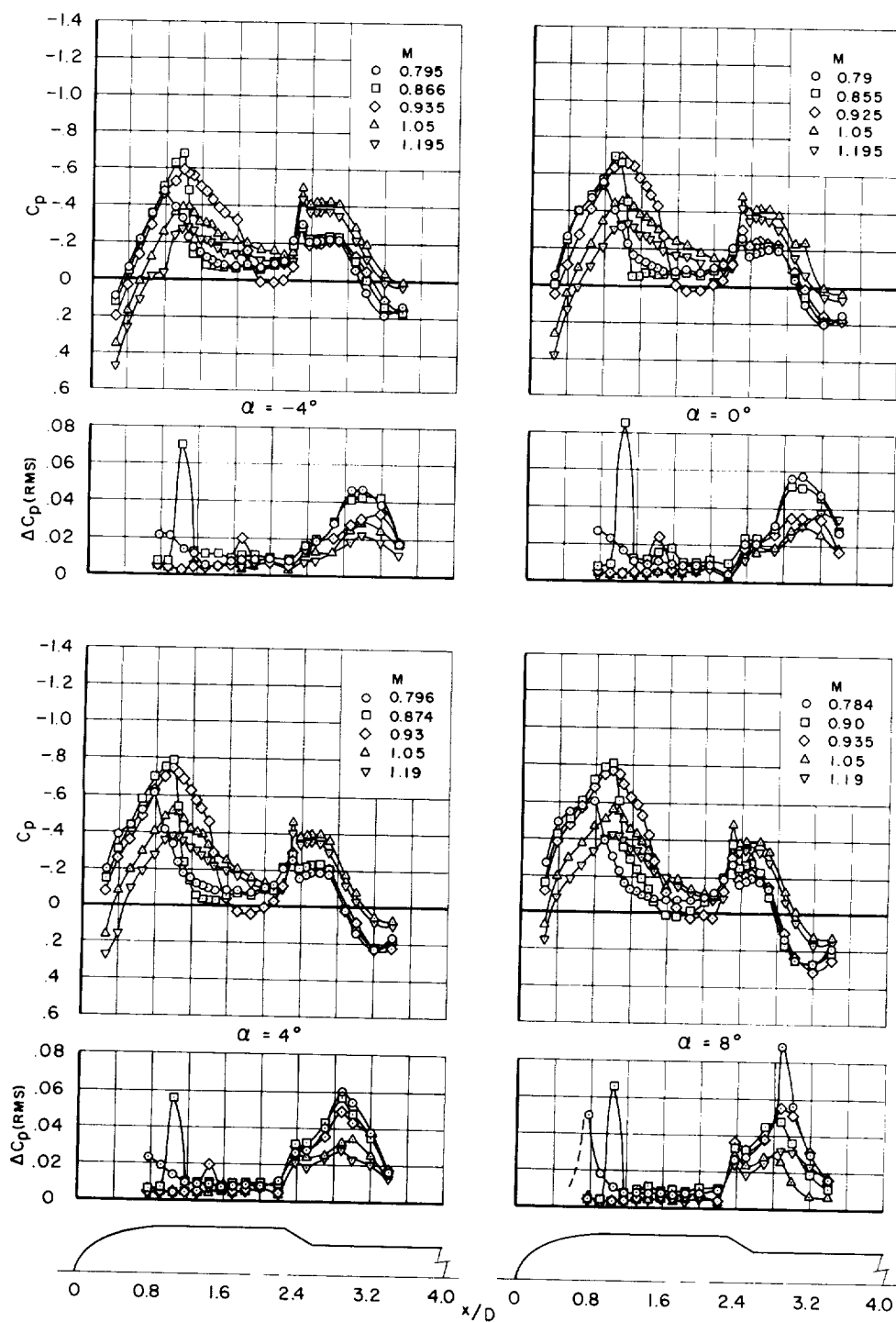
(d) Model IV.

Figure 12.- Continued.
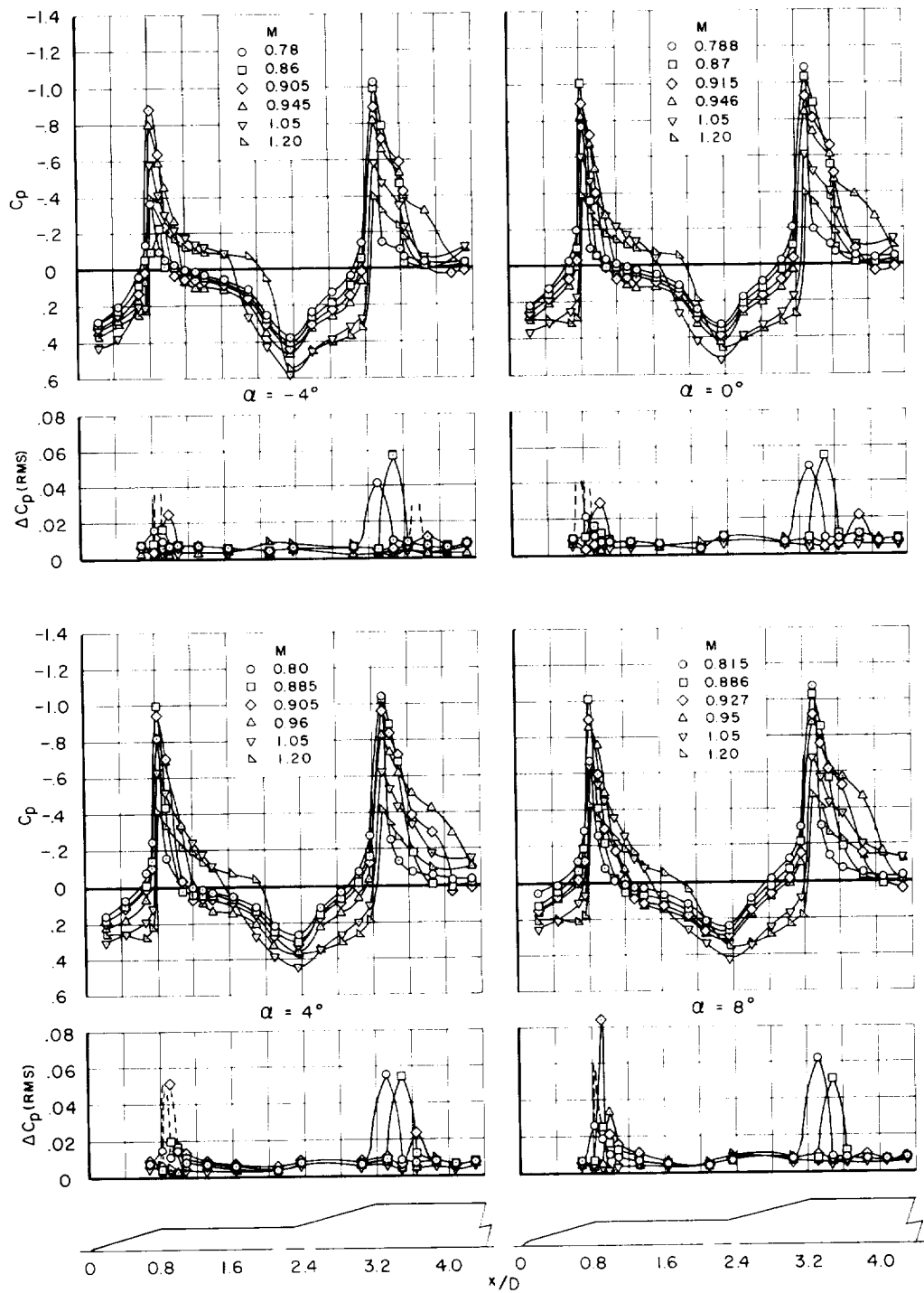
(e) Model V.

Figure 12.- Concluded.
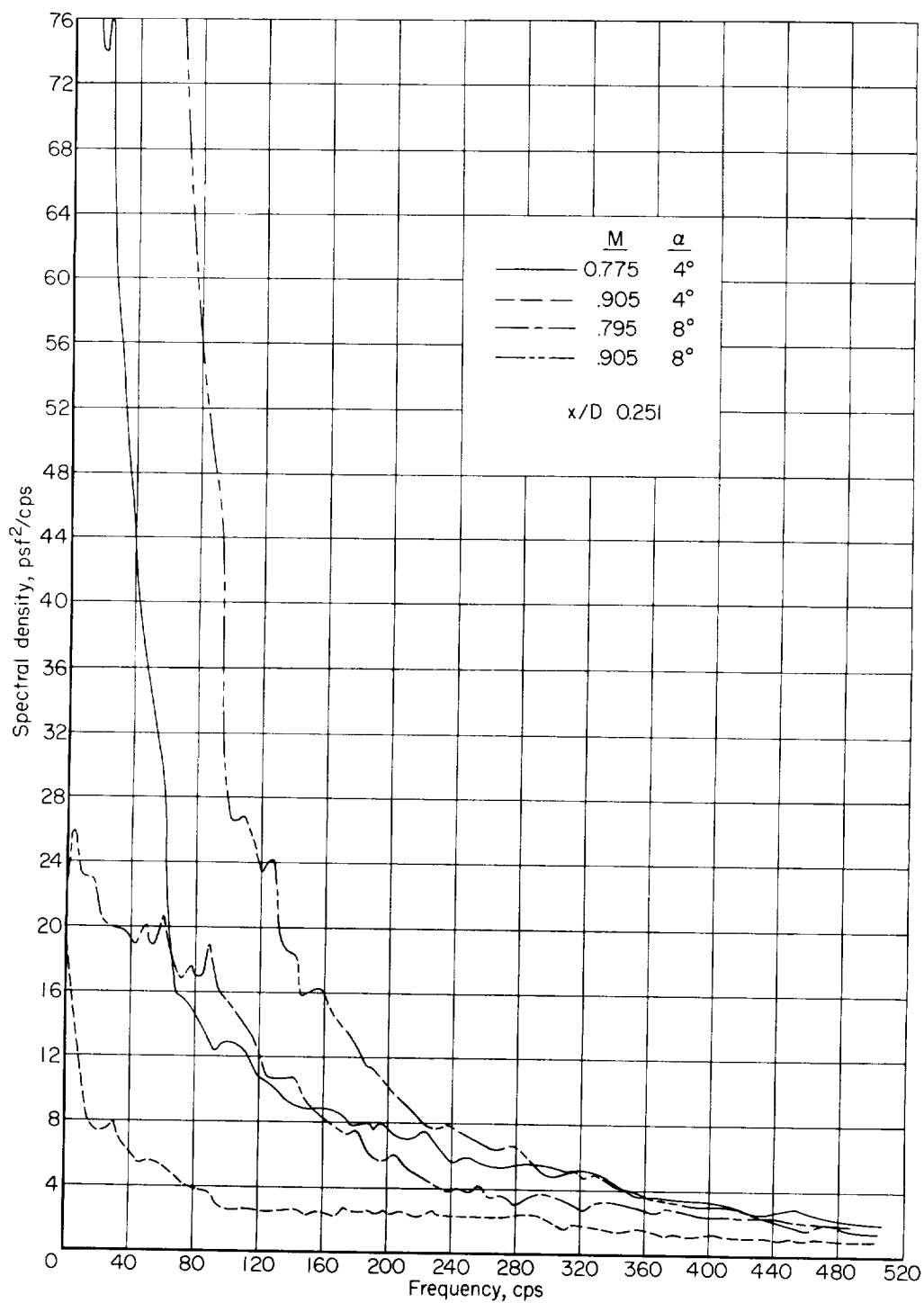
(a) x/D = 0.251

Figure 13.- Power spectral densities of pressure fluctuations on model I.
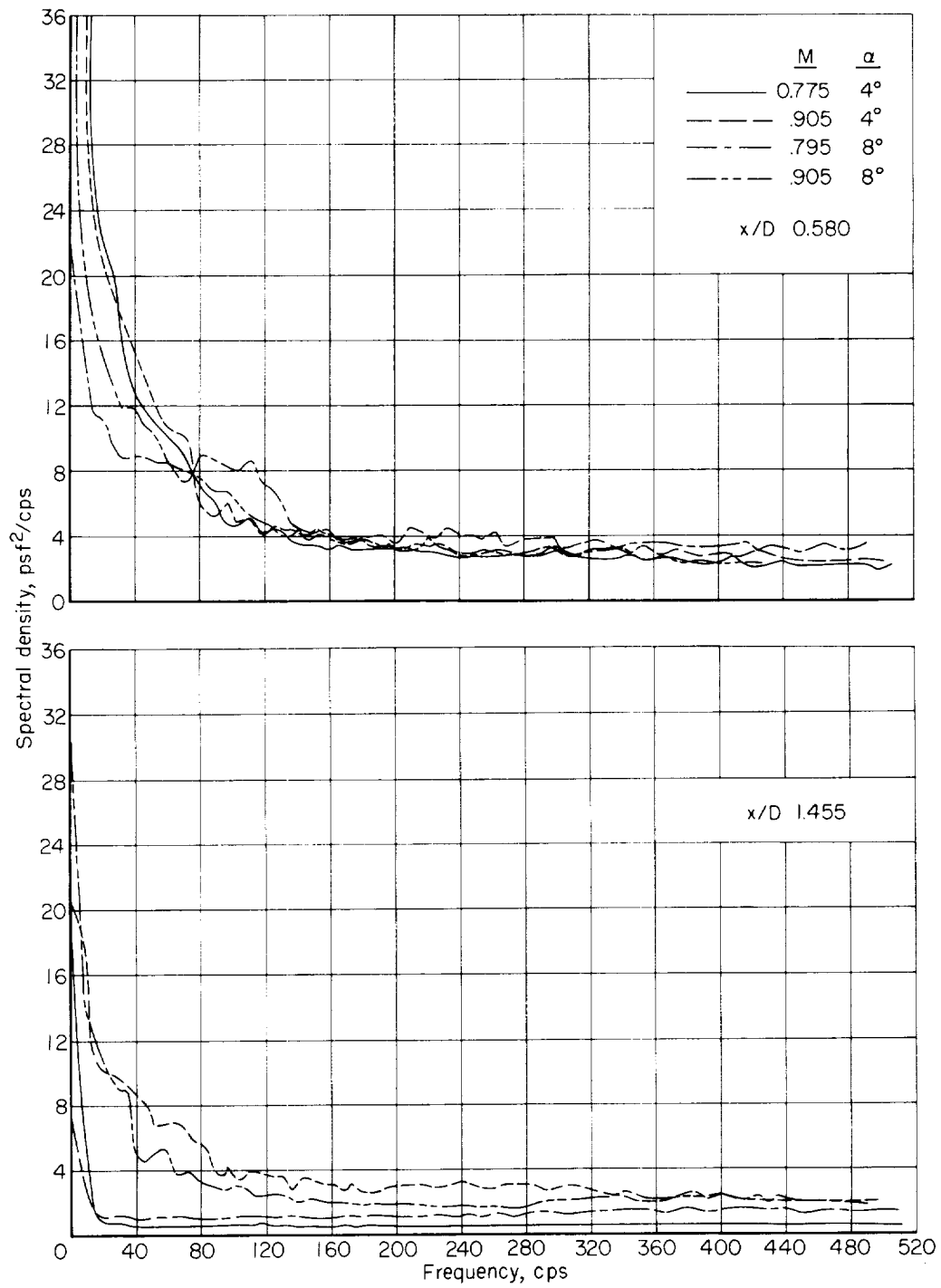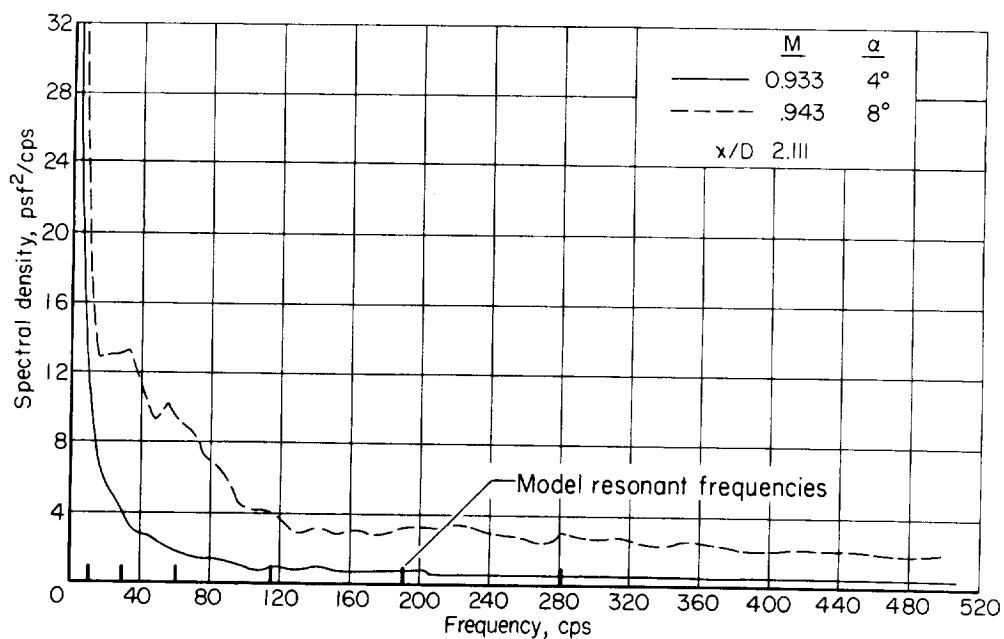
(b) x/D = 0.580 and 1.455
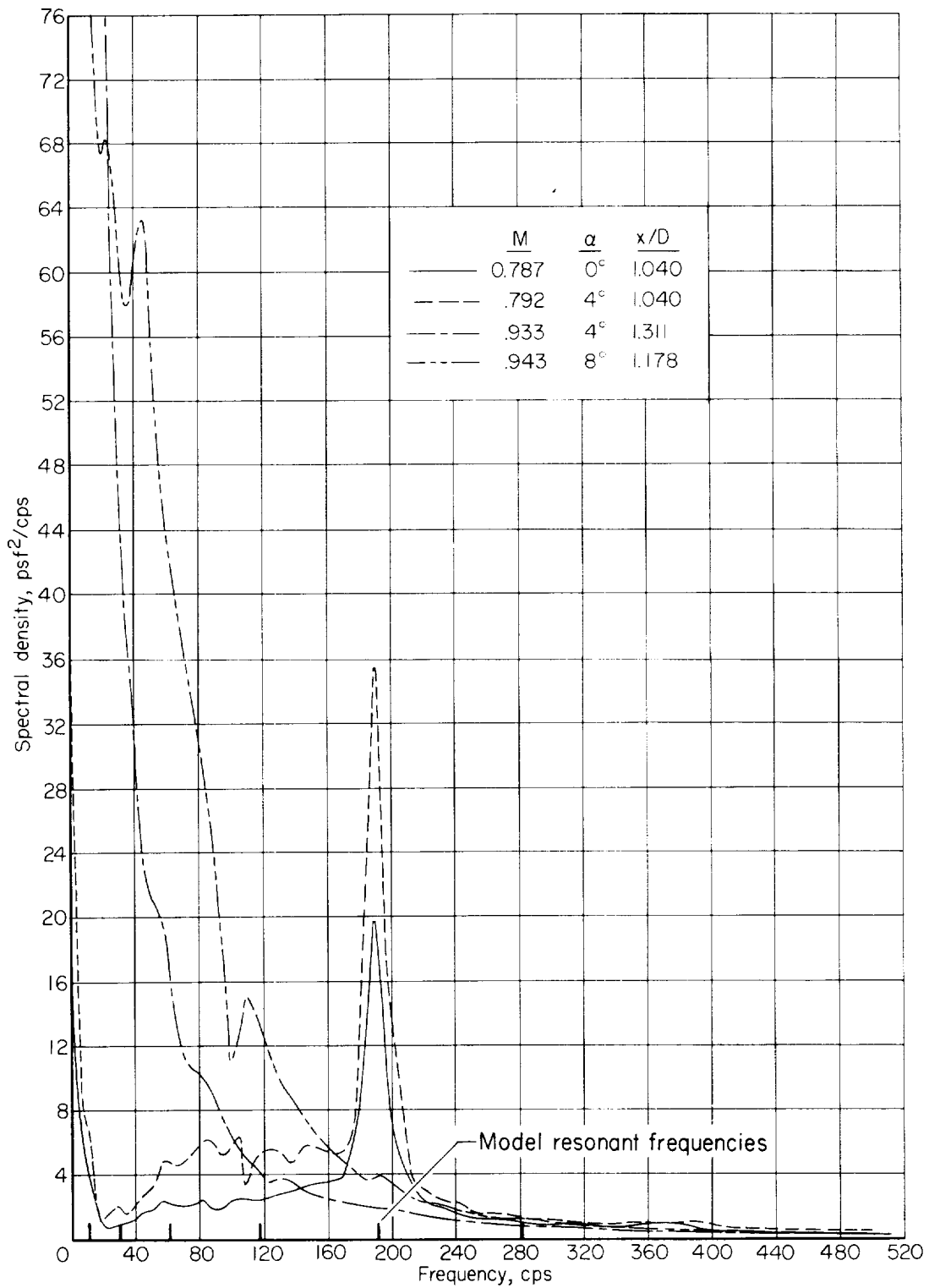
Figure 13.- Concluded.
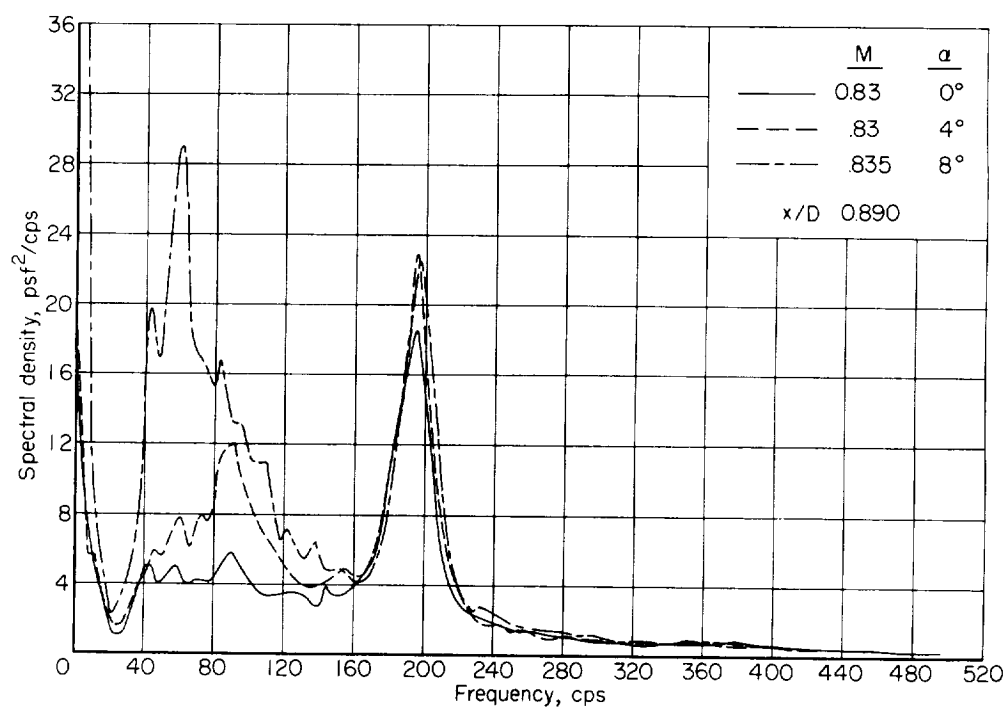
Figure 14.- Power spectral densities of pressure fluctuations on model II.

(a) Fluctuations within region of separated flow.

Figure 15.- Power spectral densities of pressure fluctuations on model III.

(b) Fluctuations within region of shock wave.
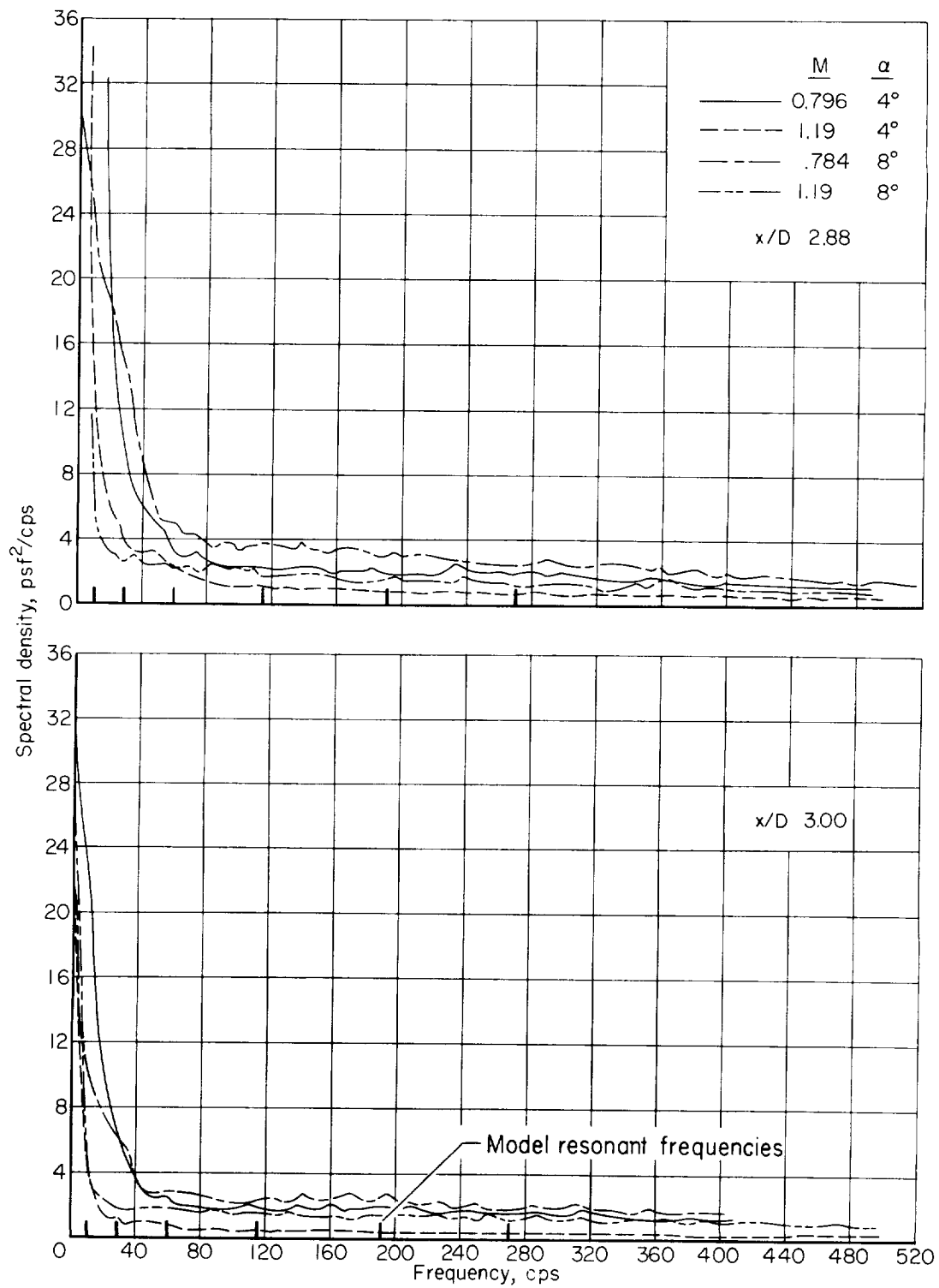
Figure 15.- Concluded.

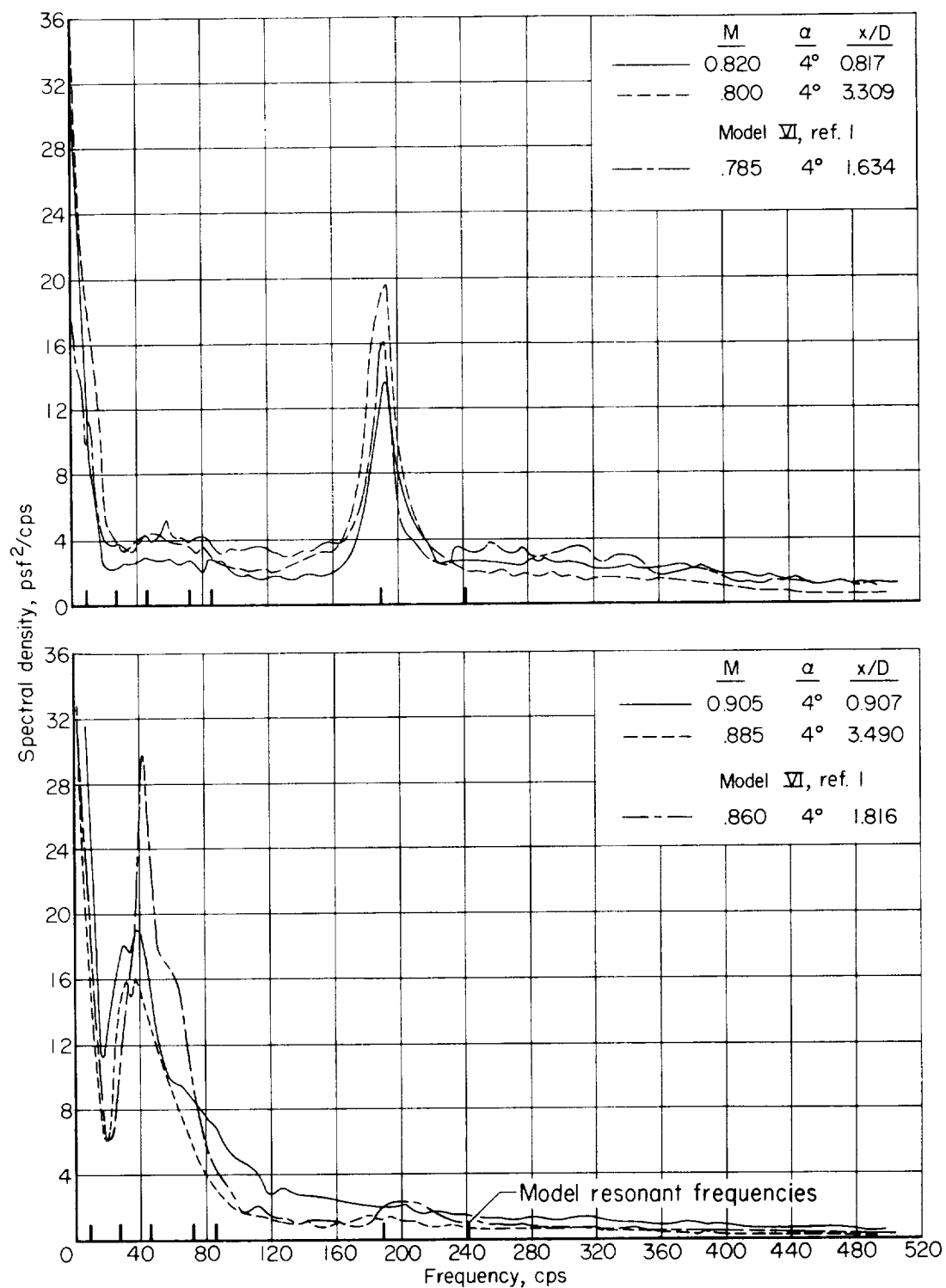Figure 16.- Power spectral densities of pressure fluctuations on model IV.

Figure 17.- Power spectral densities of pressure fluctuations on model V.